INVESTIGATION OF MULTICOLOR QUANTUM WELL INFRARED
PHOTODETECTORS AND TYPE II SUPERLATTICE INFRARED
PHOTODETECTORS

By

JUNHEE MOON

TABLE OF CONTENTS

Abstract of Dissertation Presented to the Graduate School
of the University of Florida in Partial Fulfillment of the
Requirements for the Degree of Doctor of Philosophy

INVESTIGATION OF MULTICOLOR QUANTUM WELL INFRARED
PHOTODETECTORS AND TYPE II SUPERLATTICE INFRARED
PHOTODETECTORS

By

Junhee Moon

December 2004

Chairman: Sheng S. Li
Major Department: Electrical and Computer Engineering

We developed two novel high-performance n-type quantum well infrared

photodetectors (QWIPs) for 3-5 μm mid-wavelength infrared (MWIR), and 8-14 μm long-

wavelength infrared (LWIR) detection. We simulated the InAs/GaInSb type II infrared

photodetector to get optimal detector design and demonstrated InGaAsSb photodiodes using

type II superlattice layers with different $i$ layer thickness. For infrared imaging arrays, we

also demonstrated two-color, two-stack QWIP 4 x 4 focal plane array (FPA) with dielectric

grating and fabricated a 320 x 256 FPA test structure on the GaSb substrate.

First, an InGaAs/AlGaAs two-stack three-color QWIP for MWIR and LWIR dual

band detection was presented. The LWIR TC-QWIP showed very high responsivity while

MWIR BC-QWIP had very solid photosignal at up to 200 K. The second QWIP was a new

high-sensitivity superlattice-coupled (SC) InGaAs/GaAs/AlGaAs QWIP. Excellent

responsivity and detectivity due to the use of superlattice-coupled quantum wells were

obtained and estimated, respectively.

We simulated an InAs/GaInSb type II IR detector for LWIR and VLWIR detection using two approaches: increasing the InSb mole fraction while keeping $a_s = a_{\parallel}$ and increasing the thickness ratio of constituent layers for allowing small misfit. Through simulation we proposed optimal type II IR detector designs with large valence band splitting, thin superlattice layer and large absorption coefficients. Two high-detectivity InGaAsSb *pin* IR detectors were grown on the GaSb substrate with the modified *i* layer thickness. These detectors with type II superlattice window layer have excellent responsivity and detectivity regardless of the difference in *i* layer thickness.

Finally, two-color, two-stack QWIP 4 x 4 focal plane array (FPA) with dielectric grating were fabricated and characterized. Introducing dielectric grating as light coupling improved the performance of the 4 x 4 FPA with normal incident illumination. To test the feasibility of the larger format FPAs of GaSb based type II detectors, we fabricated a 320 x 256 FPA on GaSb substrate.

CHAPTER 1
INTRODUCTION

The earliest detector dating back to the 17$^{th}$ century was liquid in a glass thermometer. Such a device was used by Herschel in 1800 [1] to demonstrate the existence of radiation beyond the red end of the visible spectrum. For the next 120 years, all of the infrared (IR) detectors developed were, like the thermometer, of the thermal detector types in that the incident radiation changed the temperature of the device and some temperature-dependent property was measured. The wide variety of semiconductor photon detectors, which have been developed over the past 80 years, for operation throughout the infrared spectrum, have brought very high sensitivity, such that in most cases the signal-to-noise ratio is determined by fluctuations in the incoming photon stream. The IR detectors are of two-types: thermal detectors and photon detectors [2]. The thermal detectors are called uncooled thermal detectors. Most thermal detectors do not require a cryogenic cooling system while the photon detectors do. Three different thermal detectors have been studied: bolometer, pyroelectric, and thermopile. Thermal detectors usually respond equally to all wavelengths but this insensitivity and slow response time significantly limits their applications. For photon detectors, the response time is very short and sensitivity is one to two orders of magnitude higher than for thermal detectors. In photon detectors, a variety of material systems such as HgCdTe, InSb, InGaAs, and PtSi have been used to detect desirable optical absorption, which has various band gap energies ($E_g$). Since the device performance of IR detectors relies heavily on quality of materials, the detector materials need stability, uniformity, and high operability. In general, the IR spectrum is divided into short-

wavelength infrared (SWIR, 1-3 μm), mid-wavelength infrared (MWIR, 3-5 μm), long-wavelength infrared (LWIR, 8-14 μm), and very long-wavelength (VLWIR, >14 μm).

The HgCdTe (MCT) is the most important semiconductor IR photon detector available for the past 4 decades. It is formed by using narrow-bandgap material HgCdTe that can yield detectivity as high as $10^{11}$ cm-Hz$^{1/2}$/W (T ≈ 80 K) and can have very large responsivity [3]. However, the MCT detectors suffer from fundamental disadvantages and limitations, such as material non-uniformity, high cost, and low-temperature operation (≤ 80 K).

Quantum well infrared photodetectors (QWIPs) based on intersubband transition schemes for detection in the MWIR and LWIR atmospheric spectral windows have been investigated extensively in recent years [4-5]. The quantum well (QW) can be formed by the conduction or the valence band offset when a smaller band gap material is grown between two larger band gap materials. The quantized energy levels are formed inside the QW, so that IR radiation can be detected because of the optical transitions from the ground state to the upper excited states. The detection wavelength of QWIP is generally not dependent on the device material but rather the layer structure including well thickness and the mole fraction of the quantum well and barrier layer materials. The rapid progress of the III-V material growth technique such as molecular beam epitaxy (MBE) [6] and metal organic chemical vapor deposition (MOCVD) has made possible the rapid development of a number of QWIP devices. The QWIP has several advantages over MCT detectors: high uniformity, high yield, low cost, wavelength flexibility, multicolor capability, radiation hardness, low 1/f noise, and large format staring arrays. The photovoltaic (PV) mode IR detector under zero bias is attractive for some applications because of the low dark current, low power

dissipation, excellent noise property, and fast integration time for focal plane array (FPA). However, the photoconductive (PC) mode under biased operation is still practical, because the responsivity of the PC mode detector is much higher than the PV mode operation.

Since the first observation of the strong optical intersubband transition in GaAs/AlGaAs multi quantum well (MQW) by West and Eglash [6] and the first demonstration of GaAs QWIP by Levine *et al.* [7]. Various intersubband transition schemes and material systems have been widely studied. For example, bound-to-bound (BT) [7], bound-to-quasi-bound (BTQB) [8], bound-to-miniband (BTM) [9], and bound-to-continuum (BTC) [10] transition schemes were chosen to improve device performance in the past decade. Figure 1.1 shows the schematic energy band diagram for various n-type QWIPs. The p-type QWIPs can allow normal incident IR detection because of their linear combination of p-like valence Bloch states without the grating coupler [4,11]. However the performance of n-type QWIP is much better. The grating coupler is no longer an issue, thanks to the advanced processing technology.

Multi-color detection for the MWIR and LWIR dual band detection is more important in determining thermal features of a target object, because the absolute temperature can be uniquely determined by the ratio of radiance measured at the two-wavelength band. Therefore, the multiple-wavelength IR detector can improve device performance, including better discrimination and tracking. Multi-color detection can be achieved by several structures: multi-stack structure with one MWIR stack and one LWIR stack [12,13]; asymmetrical QWIP structure for voltage tenability; and QWIP structure with two occupied energy levels [14]. Figure 1.1 (d) shows the multi-color QWIP using multi-stack structure.

Excellent QWIP performance allowed the development of large-format, high-sensitivity, high-speed, and low-cost QWIP staring focal plane arrays (FPAs) which are useful in some practical applications: remote sensing of earth/atmosphere, infrared astronomy, night vision, tracking, medical thermal imaging, temperature measurement, and weather watch [15]. Recently, 128 x 128, 256 x 256, and 640 x 480 FPAs [16-19] were demonstrated with higher uniformity and higher yield. Thus a 1024 x 1024 format FPA is possible now. While the multi-color QWIP FPA for MWIR and LWIR dual band detection has been successfully demonstrated, development of multi-color QWIP with high performance is of major interest for FPAs and other image applications.

Type II strained layer superlattice detectors based on GaSb have been proposed as a promising alternative for IR detectors for 3-14 μm or longer wavelength detection. Commercially available IR detectors in this spectral range can be categorized as interband detectors such as HgCdTe and InAsSb, or intersubband QWIPs. Unfortunately, some fundamental problems exist: fast Auger recombination in the interband detectors and the high thermal generation rate in intersubband detectors drastically decrease their ability for near room-temperature operation in the IR spectral range. In comparison to these detectors, type II superlattice IR detectors can have the higher effective mass of electrons and holes and a slower Auger recombination rate leading to lower dark current and higher operating temperature. Another unique and interesting feature of type II superlattices is that the superlattice band gap can be smaller than that of either of the constituent materials (Figure 1.2), making this system available up to VLWIR range.

Since it was first proposed in 1987, the InAs/GaInSb strained layer superlattice material system has undergone comparatively rapid development. Campbell *et al.* [20]

reported growth and characterization of InAs/GaInSb superlattice on GaSb substrate. They showed that infrared photo-absorption ($\lambda\sim10\mu m$) and photoconductivity are in good agreement with theoretical predictions for the photoresponse of this spatially indirect superlattice. The maximum theoretical detectivities of LWIR InAs/InGaSb superlattices were found to be greater than those of HgCdTe, provided that the comparison involves the same base-layer thickness (greater than the minority carrier diffusion length) [21-24]. Grein et al. [25] examined InAs/Ga$_{1-x}$In$_x$Sb superlattices for potential IR detector applications in the very-long-wavelength range. In p-type material, Auger recombination rates are suppressed by increasing the lattice mismatch through increasing $x$ while n-type materials are less advantageous. This suppression, particularly in the p-doped type-II superlattices, is large enough to make these material systems better device candidates than HgCdTe in the long-wavelength range ($>11\ \mu m$).

Photodiodes are generally preferred over photoconductive devices, because of power-dissipation concerns in large-area FPAs. Johnson et al. [26] reported the first investigation of heterojunction photodiodes using the InAs/GaInSb superlattice. While the electrical properties of these detectors were not yet comparable to those of HgCdTe devices, high quantum efficiencies were demonstrated in photodiodes with a turn-on wavelength of 10.6 $\mu m$ at 78K using a very thin (0.75 $\mu m$) superlattice absorbing layer. Grein and Ehrenreich introduced 11 $\mu m$ 35.9 Å InAs/15.7 Å In$_{0.225}$Ga$_{0.775}$Sb and 3.5$\mu m$ 16.7 Å InAs/35 Å In$_{0.225}$Ga$_{0.775}$Sb superlattices operating at temperatures between 200 and 300 K. They measured the combined effects of suppressing Auger recombination in superlattices, photon recycling, and the suppression of both Auger and radiative recombination with carrier depletion [27]. Though the results are better in all cases compared to their HgCdTe

counterparts, the carrier concentrations required for background limited performance are seen to be impracticably low. Mohseni *et al.* [28] reported uncooled InAs/GaSb type II IR detectors grown on GaAs substrates for the 8-12 μm atmospheric window with a responsivity of 2 mA/W at 1-V bias (E = 5 V/cm). The maximum measured detectivity of $1.3 \times 10^8$ cm·Hz$^{1/2}$ W at 11 μm and room temperature is higher than that of existing HgCdTe at 10.6 μm. To solve the problems of the GaSb substrate including high defect density, poor surface smoothness, and strong absorbance for IR radiation, a compliant GaAs substrate was introduced. Brown *et al.* [15] reported that a high photoresponse type II detector using compliant GaAs substrate, which is much advantageous in terms of cost, semi-insulating, and larger FPA applications. Further work is needed to understand and improve the quality of superlattice materials and optimal device design.

Chapter 2 describes the basic principles of quantum well infrared photodetectors, including calculation of energy levels in the quantum well and superlattice; strain effect on band structure; transfer matrix method (TMM) for calculating the transmission coefficient, the absorption coefficient on the intersubband transition in the quantum well, and the QWIP figures of merit for device performance characterization.

Chapter 3 demonstrates an InGaAs/AlGaAs two-stack three-color QWIP for MWIR and LWIR dual band detection. High responsivity (2.63 A/W at $\lambda_p$ = 10.3 μm) was obtained from LWIR TC-QWIP. A solid photosignal was found up to 200 K from MWIR BC-QWIP. Dual-band 3-color detection was demonstrated at 40 K and 77 K for the stacked detector.

Chapter 4 reports a new high sensitivity superlattice-coupled (SC) InGaAs/GaAs/AlGaAs QWIP. Excellent responsivity and detectivity have been achieved by

using SC - quantum wells, showing the possibility of further improvement through refined design.

Chapter 5 gives theoretical consideration to type II IR detectors, specifically the InAs/GaInSb strained layer superlattice detector. This chapter also includes $k \cdot p$ theory for superlattice band structure, the calculation method for strained layer superlattice, and the figures of merit for type II detectors.

Chapter 6 presents simulation of an InAs/GaInSb type II IR detector for LWIR and VLWIR detection using two approaches: increasing the InSb mole fraction while keeping $a_s$ = $a_{\parallel}$ and increasing the thickness ratio of constituent layers for allowing small misfit. Through simulations we proposed optimal type II IR detector designs with large valence band splitting, thin superlattice layers, and large absorption coefficients. However, after characterization, we found that photoconductive devices for type II IR detector were unsuccessful because of their high leakage current. We proposed the new type II IR photodiodes based on our simulation results.

Chapter 7 demonstrates two high detectivity InGaAsSb *pin* IR detectors grown on the GaSb substrate with the modified *i* layer thickness. Effects of *i* layer thickness on InGaAsSb *pin* photodiodes for SWIR detection were studied. These detectors with type II superlattice window layer have excellent responsivity and detectivity regardless of the difference in *i* layer thickness.

Chapter 8 demonstrate a two-color, two-stack QWIP 4 x 4 FPA with dielectric grating. The introduction of dielectric grating as light coupling improved the performance of the 4 x 4 FPA with normal incident illumination. We also fabricated a 320 x 256 FPA on

GaSb substrate to test the feasibility of the larger format FPAs of GaSb based type II detectors.

(a) BTC n-QWIP

(b) BTQB n-QWIP
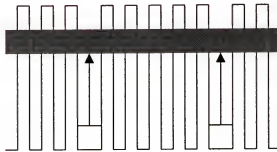
(c) BTM n-QWIP
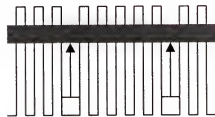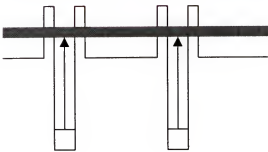
(d) 2-Color DB/BTM stacked QWIP

Figure 1.1. The schematic energy band diagrams for n-type QWIPs including multi-color QWIPs.
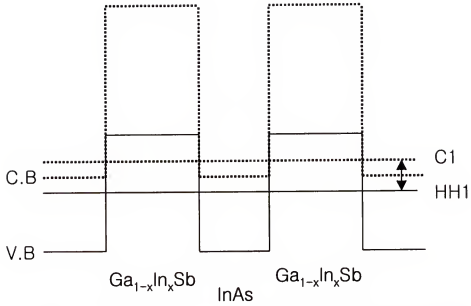
Figure 1.2. InAs/GaInSb type II staggered band line-up. $\Delta E_{c1\text{-}hh1}$ is the superlattice bandgap.

CHAPTER 2
THEORETICAL CONSIDERATIONS OF QUANTUM WELL INFRARED
PHOTODETECTORS (QWIPs)

## 2.1 Introduction

III-V semiconductor quantum well infrared photodetectors (QWIPs) based on intersubband transition schemes for detection in the 3-5 μm mid-wavelength infrared (MWIR) and 8-14 μm long-wavelength infrared (LWIR) atmospheric spectral windows have been investigated extensively in recent years [4,30]. This rapid progress in III-V semiconductor QWIPs has made it possible to develop large-area, uniform, high-performance QWIP focal plane arrays (FPAs) for staring imaging array applications [4, 31-34].

QWIPs fabricated from III-V material systems such as GaAs/AlGaAs, InGaAs/AlGaAs and InGaAs/InAlAs offer a number of potential advantages over HgCdTe(MCT) decectors. These include

- Mature GaAs growth and processing technologies

- GaAs substrates are larger, cheaper, and higher quality than MCT

- Good thermal stability

- Higher yield, lower cost, and higher reliability in III-V QWIPs than in MCT

- Better transient and total dose radiation hardness than in MCT devices.

The small electron effective mass and high electron mobility of n-type QWIPs gives them excellent IR detection properties. However, the quantum mechanical selection rule for the intersubband transition in n-type QWIPs requires that the radiation electric field has a

component perpendicular to the quantum well plane in order to induce intersubband absorption in the quantum wells. As a result, for n-type QWIPs, it is necessary to use metal or dielectric grating structure for coupling the normal incident IR radiation into the quantum well. In contrary, p-type QWIPs using normal incidence based on intervalence subband transitions have been used as an alternative, but the responsivity is found to be much smaller than those of n-type QWIPs due to the heavy effective hole mass and low mobility of holes which reduce the infrared photon absorptionin the valence band.

Using advantages of n-type QWIPs such as high detectivity, detection wavelength flexibility, and extensive research on these devices, a variety of high performance n-type QWIPs including multi-stacked multi-color QWIP [35], voltage-tunable multicolor triple-coupled QWIPs (TC-QWIPs) [36], and broadband QWIPs [37,38] have been reported in the literature.

## 2.2 Operation and Design Considerations of QWIPs

The conduction band diagram for an n-type GaAs/AlGaAs bound-to-continuum (BTC) QWIP in Figure 2.1 shows the photocurrent and the dark current. The dark current comprises three components: the thermionic emission (TE) current; the thermally assisted tunneling (TAT) current; the tunneling current. The TE current dominates at higher temperatures in the BTC QWIPs. The TAT current is the dominant current in the bound-to-miniband (BTM) QWIPs at higher temperatures. The tunneling current becomes dominant at very low temperatures for both BTC- and BTM-QWIPs. The QWIP structure is designed so that the photoexcited carriers can escape from the QWs and be collected as photocurrent. The QWIP offers greater wavelength flexibility than the impurity-doped extrinsic infrared

photoconductors, PtSi and InSb IR detectors, since the peak wavelength of a QWIP can be continuously tailored by varying the QW layer thickness and barrier composition [39]. We can calculate theoretically the peak detection wavelength as a function of the Al mole fraction, $x$, for a GaAs/Al $_x$Ga$_{1-x}$As BTC QWIP with different values of QW width, $L_w$. For example, using a 5 nm QW width, the peak detection wavelength, $\lambda_p$, will shift from 8.5 $\mu$m when the Al mole fraction, $x$, changes from 0.25 to 0.16.

Responsivity and detectivity are two key figures of merit commonly used in assessing QWIP performance. Since the performance of a QWIP depends on the dark current and responsivity, reducing the dark current and enhancing the responsivity are essential for improving the detectivity of a QWIP. Although reduced dark current and increased reponsivity can be achieved by optimizing the QW parameters and device structure, considerable efforts have also been devoted to the design of light coupling scheme in n-type QWIPs, a key factor for QWIP FPA. Several light coupling schemes are reported in the literature [4,40].

## 2.3 Energy States in Quantum Wells

Using the effective mass approximation, the quantized states in a QW can be solved from the one dimensional (1-D) time independent Schrödinger equation [41] shown in Equation 2.1,

$$\left[ -\frac{\hbar^2}{2m^*}\frac{\partial^2}{\partial z^2} + V(z) \right]\psi(z) = E\psi(z) , \tag{2.1}$$

where $\hbar = h/(2\pi)$, $h$ is the Planck's constant, $m^*$ is the effective mass, $V(Z)$ is the potential profile along $z$-direction, $\Psi$ is the eigenfunction of the energy state, $E$ is the energy eigenvalue, and $z$ is the growth direction of the QW structure.

First, we consider the quantum well structure with infinite barriers. The normalized wavefunction using the boundary conditions at $-l/2$ and $l/2$ with quantum well thickness of $l$ can be written as

$$\psi(z) = \sqrt{\frac{2}{l}} \cos\left(\frac{n\pi z}{l}\right), \quad \text{n odd} \tag{2.2}$$

$$\psi(z) = \sqrt{\frac{2}{l}} \sin\left(\frac{n\pi z}{l}\right), \quad \text{n even .} \tag{2.3}$$

For the quantum well structure with finite barrier height ($V_c$), the condition of the allowed bound energy states can be obtained as

$$\begin{aligned} \alpha \tan\left(\frac{\partial l}{2}\right) &= \beta, \\ \alpha \cot\left(\frac{\partial l}{2}\right) &= -\beta, \end{aligned} \tag{2.4}$$

where

$$\begin{aligned} \alpha &= \sqrt{\frac{2m^* E}{\hbar^2}}, \\ \beta &= \sqrt{\frac{2m^*(V_c - E)}{\hbar^2}}. \end{aligned} \tag{2.5}$$

Thus, the above equations can be solved by numerical technique.

In superlattice structure, which is alternatively and periodically repeated by the quantum wells and thin barriers, bound state wavefunctions can be overlapped and form a miniband. Using the Kronig-Penney model, the dispersion relation of the minibands can be obtained. If the superlattice has a quantum well width of $a$, barrier width of $b$, barrier height of $V_c$, and period of $d$ ($= a+b$), the solution of the Schrödinger equation for this superlattice can be expressed as a Bloch state wavefunction , which is given by

$$\psi(z+d) = e^{ik_z d}\psi(z) \quad . \tag{2.6}$$

In a period,

$$\psi(z) = Ae^{i\delta z} + Be^{-i\delta z}, \text{ in the barrier} \tag{2.7}$$

$$\psi(z) = Ce^{i\alpha z} + De^{-i\alpha z}, \text{ in the well.} \tag{2.8}$$

And in the next period,

$$\psi(z) = e^{ik_z d}\left[Ae^{i\delta(z-d)} + Be^{-i\delta(z-d)}\right], \text{ in the barrier} \tag{2.9}$$

$$\psi(z) = e^{ik_z d}\left[Ce^{i\alpha(z-d)} + De^{-i\alpha(z-d)}\right], \text{ in the well} \tag{2.10}$$

where A, B, C, and D are constants which can be obtained by using the boundary conditions and the dispersion relations for the bound and unbound states are given as [42]

$$\cos(k_z d) = \cos(a\alpha)\cosh(b\beta) - \frac{\alpha^2 - \beta^2}{2\alpha\beta}\sin(a\alpha)\sinh(b\beta), \text{ for } 0 < E < V_c, \tag{2.11}$$

$$\cos(k_z d) = \cos(a\alpha)\cosh(b\delta) - \frac{\alpha^2 + \delta^2}{2\alpha\delta}\sin(a\alpha)\sinh(b\delta), \text{ for } E > V_c. \tag{2.12}$$

The energy level of minibands can then be solved from the above equations.

## 2.4 Transfer Matrix Method (TMM) for the Transmission Coefficient

To solve the Schrödinger equation with an arbitrary potential function, many different approaches [43-46] have been used such as the standard analytical method, Wentzel-Kramers-Brillouin (WKR) approximation, Kronig-Penney model, and the variational principle, which are however not suitable for general purposes. Recently the transfer matrix method (TMM) [47], which provides the straightforward multiplication of 2 x 2 matrices with no iterations, has been developed to analyze exactly the multi-quantum well structures. If we consider an arbitrary multi-quantum well structure with $N+1$ layers, the solution of the Schrödinger wave equation can be given as

$$\psi_n = A_n e^{-i\Delta_n} e^{ik_n z} + B_n e^{i\Delta_n} e^{-ik_n z}, \qquad (2.13)$$

where

$$\Delta_1 = \Delta_2 = 0, \qquad (2.14)$$

$$\Delta_n = k_n(d_1 + d_2 + \cdots + d_{n-1}), \quad n = 3, 4, 5, \cdots, N+1 \qquad (2.15)$$

$$k_n \left[ \frac{2m_n^*}{\hbar^2}(E - V_n) \right]^{1/2}, \qquad (2.16)$$

where $A_n$ and $B_n$ are the amplitudes of the wave function in $+z$ and $-z$ directions, respectively, and $d_n$, $m_n^*$, and $V_n$ are the thickness, the effective mass, and the potential of the $n^{th}$ layer, respectively. Applying the boundary conditions at each interface gives as follows

$$\begin{pmatrix} A_1 \\ B_1 \end{pmatrix} = S_1 \begin{pmatrix} A_2 \\ B_2 \end{pmatrix} = S_1 S_2 \begin{pmatrix} A_3 \\ B_3 \end{pmatrix} = \cdots = S_1 S_2 \cdots S_N \begin{pmatrix} A_{N+1} \\ B_{N+1} \end{pmatrix}, \qquad (2.17)$$

where N is the total number of the layers and

$$S_n = \frac{1}{t_n} \begin{pmatrix} e^{-ik_n d_n} & r_n e^{-ik_n d_n} \\ r_n e^{ik_n d_n} & e^{ik_n d_n} \end{pmatrix}, \quad r_n = \frac{k_n - k_{n+1}}{k_n + k_{n+1}}, \quad t_n = \frac{2k_n}{k_n + k_{n+1}}. \qquad (2.18)$$

We can set $B_{N+1} = 0$ since there is no reflection wave in the $(n+1)^{th}$ layer. As a result, the transmission coefficients can be obtained by $|A_{n+1}/A_1|^2$ as a function of energy $E$ and then each energy states can be obtained.

## 2.5 Strain Effects on the Energy Bandgap

Strained-layer heterostructures allow the use of lattice-mismatched materials without the generation of misfit dislocations if the layer thickness is less than the critical thickness (Fig. 2.2) [48-53]. This freedom from the need for precise lattice matching widens the choice

of compatible materials and greatly increases the ability to control the electronic and optical properties of the strained-layer structures.

Strain effects induced by lattice-mismatch will modify the energy band structure. From the elasticity theory [54], the biaxial strain can be divided into two independent components: one is isotropic or hydrostatic component and the other is anisotropic or shear uniaxial component. The strain-induced energy shifts, $\Delta E_H$ due to the hydrostatic component and $\Delta E_U$ due to the shear uniaxial component [55], can be expressed, respectively, by

$$\Delta E_H = 2V_{cd} \frac{C_{11} - C_{12}}{C_{11}} \delta_0 , \qquad (2.19)$$

$$\Delta E_U = V_{sd} \frac{C_{11} + 2C_{12}}{C_{11}} \delta_0 , \qquad (2.20)$$

where $V_{cd}$ and $V_{sd}$ are the conduction-band deformation potential and shear deformation potential, respectively, $C_{ij}$ are the elastic constants, and $\delta_0$ is the lattice-mismatch strain, $\delta_0 = (a_s - a)/a$ where $a_s$ and $a$ are the lattice constants of the substrate and the strained-layer, respectively. The energy bandgaps due to the strain for the heavy-hole and light-hole states [55] at $k = 0$ are given by

$$\left( E_g^{C,HH} \right)_s = \left( E_g^0 \right)_s + \Delta E_H - \Delta E_U , \qquad (2.21)$$

$$\left( E_g^{C,LH} \right)_s = \left( E_g^0 \right)_s + \Delta E_H + \Delta E_U - \frac{(\Delta E_U)^2}{2\Delta_o} + \cdots , \qquad (2.22)$$

where $\left( E_g^0 \right)_s$ is the unstrained bandgap and $\Delta_o$ is the spin-orbit splitting energy. The band-offsets of the conduction and valence band of the heterostructure can be calculated by

$$\begin{aligned} \Delta E_C &= Q_C \Delta E_g , \\ \Delta E_V &= Q_V \Delta E_g \end{aligned} \qquad (2.23)$$

where $Q_C$ and $Q_V$ are the band offset ratios of the conduction and valence bands, respectively, and $\Delta E_g$ is the energy gap discontinuity of the barrier and well materials.

## 2.6 Absorption Coefficient on Intersubband Transition in Quantum Wells

The calculation of the absorption coefficient on intersubband transition in a QW structure is needed to determine the absorption strength and the absorption lineshape. The linear intersubband absorption coefficient within the conduction band of the quantum well can be expressed as [56]

$$\alpha(\omega) = \omega \sqrt{\frac{\mu_0}{\varepsilon}\left(\frac{q^2 m^* kT}{L_w \pi \hbar^2}\right)} \sum_{m>n} \left[ \begin{array}{c} |M_{mn}|^2 \times \ln\left(\dfrac{1+\exp[(E_F - E_n)/kT]}{1+\exp[(E_F - E_m)/kT]}\right) \\ \times \dfrac{(\hbar/\tau)^2}{(E_m - E_n - \hbar\varpi)^2 + (\hbar/\tau)^2} \end{array} \right] , \qquad (2.24)$$

where $\mu_0$ is the permeability in vacuum, $\varepsilon$ the dielectric constant, $L_w$ the total quantum well width, $\tau$ the lifetime, $E_F$ the Fermi level of the system. The dipole matrix element $M_{mn}$ is given by

$$M_{mn} = \int_{L_w/2}^{+L_w/2} \psi_m^*(z)|z|\psi_n(z)dz . \qquad (2.25)$$

The integrated absorption strength is given by

$$I_A = \int_0^\infty \alpha(w)dw \qquad (2.26)$$

and the dipole oscillator strength is given by

$$f_{os} = \frac{4\pi m^* c}{\hbar\lambda}|M_{mn}|^2 . \qquad (2.27)$$

The Fermi level $E_F$ can be calculated from [13]

$$N_d = \frac{m^* kT}{\pi \hbar^2 L_w} \sum_n \ln\left[1 + \exp\left(\frac{E_F - E_n}{kT}\right)\right] . \qquad (2.28)$$

It is noted that $N_d$ expression is valid for summation over subband levels $E_n$ below the Fermi level $E_F$. It is noted from Eq. (2.25) that the normal incidence radiation for $n$-type QWIPs will not be absorbed because there is no electric field component along the z-axis. Therefore, both 45° polished facet illumination and grating coupler [57-59] have been used to characterize the performance of $n$-type QWIPs.

## 2.7 Figures of Merit

In designing a quantum well infrared photodetector (QWIP), it is important to understand the key parameters that determine the performance of a QWIP. These parameters, which are often called the figures of merit, include dark current $I_d$, noise equivalent power ($NEP$), responsivity ($R$), and detectivity ($D^*_\lambda$).

### 2.7.1 Dark Current $I_d$

In a quantum well infrared photodetector, the dark current is due to both the thermionic emission and tunneling conduction. For a conventional QWIP, thermionic emission conduction is dominant at high temperatures, whereas in a BTM QWIP thermionic-assisted tunneling conduction through the miniband is dominant. In the low-field regime, the thermionic emission current is given as [60]

$$I_{th} = A_d e v_d n_t, \tag{2.29}$$

where $A_d$ is the detector active area, $v_d$ is the average drift velocity, and $n_t$ is the density of mobile carriers. Here, $v_d$ and $n_t$ are given as follows

$$v_d = \frac{\mu F}{[1 + (\mu F / v_s)^2]^{\frac{1}{2}}}, \tag{2.30}$$

$$n_t = (m^* k_B T / \pi \hbar^2 L) \exp[-(E_{cut} - E_F)/(k_B T)], \tag{2.31}$$

where $v_s$ is the saturation drift velocity, $E_{cut}$ is the cutoff energy related to the cutoff wavelength $\lambda_c$, and $m^*/\pi\hbar^2$ is the 2-dimensional (2-D) density of states. In the above equation, the Fermi level $E_F$ can be obtained from

$$N_D = \frac{m^* k_B T}{\pi \hbar^2 L_a} \sum_n \ln[1 + \exp(\frac{E_F - E_n}{k_B T})], \tag{2.32}$$

$$\approx \frac{m^*}{\pi \hbar^2 L_a} \sum_n (E_F - E_n). \tag{2.33}$$

Eq. (2.33) is a simplified expression at cryogenic temperature, in which the thermionic emission current varies exponentially with the doping concentration in the quantum well at the cryogenic temperature,

$$I_{th} \propto e^{E_F / k_B T} \propto e^{C N_D /(k_B T)}, \tag{2.34}$$

where $C$ is a constant. From Eq. (2.34), it is noted that a trade-off between the dark current density and the doping concentration is required for high performance QWIP because the dark current increases exponentially with doping concentration in the well while the intersubband absorption is increased with increasing doping density.

### 2.7.2  Spectral Responsivity $R$

The responsivity ($R_A$) for the PC mode QWIP is defined by the photocurrent output (in ampere) under IR radiation power (in watt) at a specific wavelength. The responsivity depends on the detector quantum efficiency $\eta$ and the photoconductive gain $G$, and can be written as [61]

$$R_A = \frac{e}{h\upsilon}(\eta \cdot G) = \frac{e}{h\upsilon}\eta_c = \frac{\lambda}{1.24}\eta_c, \tag{2.35}$$

where

$$\eta = \kappa (1 - R_f)(1 - e^{-m l \beta}).$$

(2.36)

Here $R_f$ is the reflection coefficient ($\approx 0.3$ for GaAs), $\kappa$ is the polarization correction factor ($\kappa = 0.5$ for n-type QWIP and $\kappa = 1$ for p-type QWIP), $m$ is the number of abrorption pass, $\alpha$ is the absorption coefficient for the superlattice, and $l$ is the total superlattice thickness. The spectral responsivity (V/W) for the PV mode QWIP can be obtained from the relatioiship $R_v = R_A \cdot R_d$, where $R_d$ is the differential resistance of a QWIP.

### 2.7.3 Collection Efficiency $\eta_c$

The QWIP collection efficiency is defined as the product of the quantum efficiency $\eta$ and photoconductive gain G ($\eta_c = \eta \cdot G$), which means the converting efficiency from incident radiation photons to net carriers that are collected at the output of the QWIP. Here, the photoconductive gain G is the ratio of the carrier transport lifetime $\tau_L$ to the transit time $\tau_T$ through a QWIP and can be expressed in terms of the capture or trapping probability $P_c$ defined as the ratio of the escaping time in the well region to the lifetime of the excited carriers from the confined ground states [62,63]

$$G = \frac{\tau_L}{\tau_T} = \frac{1 - P_c}{N P_c}.$$

(2.37)

For minimizing the trapping probability and maximizing the photoconductive gain, the escaping time should be reduced in such a way that the excited states are resonantly lined up with the top of the barrier. The final expression for $\eta_c$ is decsribed by

$$\eta_c = A(1 - R)(1 - e^{-B \alpha l_{qw}}) \frac{1 - P_c}{P_c}$$

$$\approx A(1-R)\frac{B\alpha l_{qw}}{NP_c}, \quad \text{for } B\alpha l_{qw} \ll 1 \text{ and } P_c \ll 1 \quad (2.38)$$

where $A$ is a constant depending on the polarization dependence of the detector, for $n$-QWIP, $A = 1/2$, and for $p$-QWIP, $A = 1$, $\alpha$ is the absorption coefficient of the quantum well, $l_{qw}$ is the total width of all the QWs, $R$ is the reflection coefficient, and $B$ is the number of paths of light through the photodetector.

### 2.7.4 Noise Characteristics of a QWIP

The noise in a QWIP may be attributed to the following sources :

(1) Thermal noise (Johnson-Nyquist noise) due to the random motion of electrons,

(2) Generation-recombination ($g$-$r$) noise due to fluctuation in the number of electrons thermally excited into the excited states,

(3) Photon noise due to fluctuation in the number of photon excited electrons into the excited states, and

(4) 1/f noise whose power varies inversely with frequency.

The thermal noise current is given as

$$i_{thermal}^2 = 4k_B TG\Delta f, \quad (2.39)$$

where $\Delta f$ is the bandwidth, $G = (\partial I/\partial V)$ is the conductance per unit area of the device.

Since QWIP is a majority carrier device, both the $g$-$r$ noise and photon noise for background temperature less than 300°K can be expressed as

$$i^2 = 4I^2\frac{\tau}{\Delta N}\frac{\Delta f}{1+\omega^2\tau^2}, \quad (2.40)$$

where $I$ is the current flowing across a QWIP device, $\omega = 2\pi f$ is the angular frequency, $\Delta N$ is the number of thermally or photo-excited electrons. Eq.(2.40) can also be rewritten as

$$i^2 = 4egI \frac{\Delta f}{1 + \omega^2 f^2} \,. \tag{2.41}$$

Therefore, the total noise in a QWIP is given by

$$i^2 = i_{thermal}^2 + i_{g-r}^2 + i_{ph}^2 \,, \tag{2.42}$$

where $i^2_{thermal}$ is given in Eq.(2.39), $i^2_{g-r} = 4egI_{th}[\Delta f/(1+\omega^2\tau^2)]$ and $i^2_{ph} = [\Delta f/(1+\omega^2\tau^2)]$,

in which $i_{thermal}$, $i_{g-r}$, and $i_{ph}$ represent thermal noise, g-r noise, and photon noise, respectively.

Here, $I_{th}$ is the dark current given by Eq.(2.29) and $I_{ph}$ is the photo-current due to background

radiation generated electrons given as

$$I_{ph} = e\eta g \Phi_b A \,, \tag{2.43}$$

where $\Phi_b$ is the background incident photon flux and defined as

$$\Phi_b = \frac{2\pi}{c^2} \frac{f^2 \Delta f}{\exp(hf/k_B T_b) - 1} \sin^{2(\frac{\theta}{2})} \,, \tag{2.44}$$

where $T_b$ is the background temperature, $\theta$ is the angle termed as a field of view, and $\Delta f$ is

the noise spectral width.

The detectivity $D^*_\lambda$ may be expressed as [10,64]

$$D^*_\lambda = \frac{e\eta g}{h\nu i_n} (A \Delta f)^{\frac{1}{2}} \,, \tag{2.45}$$

where $A$ is the detector area, $\Delta f = 1$ Hz, and $i_n$ is the noise current from QWIP.


## 2.7.5 Background Limited Performance BLIP

For a mid-wavelength (MW) or long-wavelength (LW) QWIP there are two kinds of

backgrounds:

(1) high temperature ambient background (T = 300K) and

(2) low temperature cold background (T = 77 or 195K). Under the normal thermal imaging condition, the total current feeding to the readout circuits in a QWIP includes both the dark current $I_d$ and 300K background photocurrent $I_b$(i.e., $I_d + I_b$). Due to the limitation on the charge handling capacity in the readout circuits, the total current level of a QWIP under proper operation condition must be below this limited charge capacity for a given intergration time of the imaging arrays. In addition, in order to achieve the stable and clear imaging patterns, it is highly desirable to operate QWIPs under the background photon noise limitation, that is the background limited performance (BLIP).
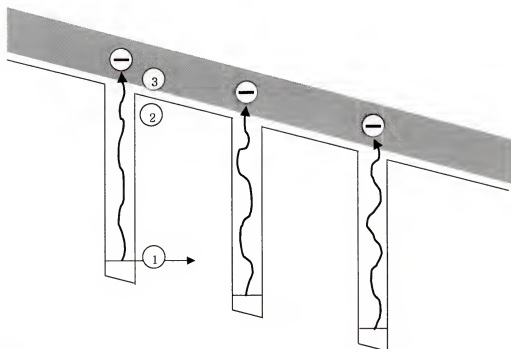
Figure 2.1. Photocurrent and dark current in a bound-to-continuum (BTC) transition QWIP
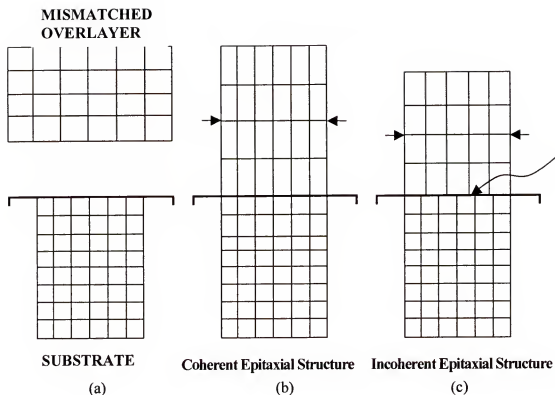
Figure 2.2. (a) A strained later structure is formed by forcing a mismatched overlayer into interfacial coherence with a substrate. When below the critical thickness for strained later stability, the resulting coherent structure is shown in (b). If the overlayer is thick enough that the coherent structure is unstable, the mismatch will partially be accommodated by lattice strain and partially by introduction of misfit dislocations (c).

CHAPTER 3
2-STACK, 3-COLOR QWIP FOR MID- AND LONG-WAVELENGTH INFRARED
DETECTION

### 3.1 Introduction

Since the first realization of quantum well infrared photodetectors (QWIPs) in 1987

[7] QWIPs based on intersubband transitions have been widely investigated for detection

in the 3-5 μm mid-wavelength infrared (MWIR) and 8-14 μm long-wavelength infrared

(LWIR) wavelength bands using III-V semiconductor material systems grown by the

mature MBE technique [4]. Of various research approaches in QWIP technology, Multi-

color QWIPs using different transition schemes and structures have been successfully

demonstrated in recent year [4]. Theoretical studies of quantum-confined Stark effect in

two- and three-coupled-quantum-well (TCQW) reported by Y. Huang *et al.* [65,66]

paved the way for realization of voltage-tunable multicolor triple-coupled QWIPs (TC-

QWIPs) for 8-12 μm long-wavelength detection [32,67]. This high-strain

InGaAs/AlGaAs/InGaAs TC-QWIP has shown excellent performance and wavelength

tenability in the LWIR spectral range [67]. While most QWIP devices were developed

with sensitivity in the 3-5 μm MWIR or 8-12 μm LWIR region, the multi-color QWIPs

were mainly investigated by using multi-stack quantum well structure for both the mid-

and long-wavelength detection at the same time or voltage tuning of peak wavelength

such as TC-QWIP, which usually has narrow bandwidth due to bound-to-bound state

transition [32,67]. These multi-color QWIPs can give a great advantage in

implementation of multi-color Focal Arrays (FPAs) since it does not need multiple layers of detectors.

In this chapter, we report a high performance two-stack, three-color high-strain InGaAs/AlGaAs/InGaAs asymmetrical triple-coupled (TC-) and InGaAs/AlGaAs bound-to-continuum (BC) QWIP grown on GaAs substrates for long-wavelength infrared (LWIR) and mid-wavelength infrared (MWIR) dual band detection

### 3.2 Device Design and Fabrication

A multi-color two-stack high-strain InGaAs/AlGaAs/InGaAs LWIR TC-QWIP and an InGaAs/AlGaAs MWIR BC-QWIP grown on GaAs substrate has been fabricated and characterized. The top stack is for LWIR detection which composes of a 5.5 nm deep $In_{0.25}Ga_{0.75}As$ quantum well Si-doped to $N_d = 7 \times 10^{17}$ $cm^{-3}$, two undoped 4 nm shallow $In_{0.12}Ga_{0.88}As$ quantum wells, and two 2 nm $Al_{0.08}Ga_{0.92}As$ inner barriers between 50 nm thick $Al_{0.08}Ga_{0.92}As$ barriers as a unit cell. The unit cell was repeated 20 times, and was sandwiched between two undoped 100 nm GaAs spacer layers to reduce the tunneling current from the contacts to the QWs. The bottom stack for the MWIR QWIP consists of 3-period of symmetrical $In_{0.3}Ga_{0.7}As/Al_{0.3}Ga_{0.7}As$ (4.3 nm / 30 nm) BC-QWIP structure. Finally, the ohmic contact layers (Si-doped to $n = 2 \times 10^{18}$ $cm^{-3}$) were grown on the top of the LWIR stack and on the bottom of the MWIR stack, and between the two stacks. Table 3.1 lists the layer structure of this high- strain multi-color two-stack QWIP structure.

Figure 3.1 shows the schematic conduction band diagram and the intersubband transition scheme for the stacked LWIR TC-QWIP and MWIR BC-QWIP. For the LWIR TC-QWIP, the 50 nm thick $Al_{0.08}Ga_{0.92}As$ barrier will turn into a triangular barrier for the conduction of

the photo-generated carriers through them when the negative bias voltage is large enough. Therefore, both the bound-to-bound (B-B) and bound-to-continuum (B-C) transitions can be detected at higher negative bias voltages. The photo-excited electrons from the $E_1$ to $E_c$ (bound-to-continuum) states contribute to the photocurrent for the MWIR BC-QWIP.

The test mesa structure with an active area of $216 \times 216 \ \mu m^2$ was fabricated to characterize the device performance by using standard photolithography and wet chemical etching procedure. The LWIR TC- QWIP and stacked-QWIP test devices were etched from the top contact layer onto the middle and the bottom contact layers, respectively. The MWIR BC-QWIP was etched from the middle contact layer into the bottom contact layer after both the top contact layer and the LWIR stack were completely removed. The LWIR TC- QWIP and stacked-QWIP test devices were annealed at $T = 450^o$C for two minutes after AuGe/Ni/Au (300Å/100Å/1000Å) deposition. The MWIR BC-QWIP test device was annealed at $T = 450^o$C for 10 seconds after AuGe/Ag/Au (300Å/1000Å/1500Å) evaporation. The $45^o$ facet was polished on the GaAs substrate for backside IR illumination. The dark I-V and spectral responsivity curves were measured for this two-stack device, and the results are described follows.

## 3.3 Dark Current Measurements

### 3.3.1 The 20-Period LWIR TC-QWIP

Figure 3.2 shows the dark current versus bias voltage (I-V) curves for the LWIR TC-QWIP measured at $T = 40, 60$, and 77K along with the 300 K background window current at $180^o$ field of view (FOV). The LWIR TC-QWIP is under background limited performance

(BLIP) when the applied bias is between −8V and +7V at $T_{BLIP}$ = 40K, and between -4V and +2.5V at $T_{BLIP}$ = 60K.

### 3.3.2 The 3-Period MWIR BC-QWIP

Figure 3.3 shows the dark current versus bias voltage (I-V) curves of the MWIR BC-QWIP measured at T = 40, 77, 100, and 120 K along with the 300 K background window current at 180° field of view (FOV). The MWIR BC-QWIP is under background limited performance (BLIP) when the applied bias is between −0.95V and +0.9V at T = 77 K. The BLIP temperature is around T = 90 K for −0.5V<$V_b$<0.4V.

### 3.3.3 The Stacked-QWIP

Figure 3.4 shows the dark current versus bias voltage (I-V) curves for the stacked-QWIP measured at T = 40, 60, and 77K. The 300K window current with 180° field of view (FOV) is also shown in Figure 4. The stacked-QWIP is also under BLIP in the entire range of the applied bias voltages (-9V<$V_b$<8V) at T = 40K while this device is under BLIP for biases between −5V and 3V at T = 60K.

### 3.4 Photoresponse Measurements

The spectral response was measured at T = 40 K for the LWIR TC-QWP, and at T = 40, 77, 100, and 120 K for the MWIR BC-QWIP, and T = 40 and 77K for the stacked-QWIP by using an I/8 monochromater, a calibrated blackbody IR source (T = 1273 K), and an Oxford CCC1204 closed cycle liquid helium cryostat at 200 Hz chopped frequency.

### 3.4.1 The 20-Period LWIR TC-QWIP

Figure 3.5 shows the spectral responsivity of the LWIR TC-QWIP measured at different bias voltages and T = 40K. As a result of the switched location between AlGaAs deep quantum well and InGaAs shallow wells compared to the previously reported TC-QWIP structures [36,67], the bound-to-continuum (B-C) transitions can be detected under the positive and lower negative bias voltages while the bound-to-bound (B-B) transitions were observed at higher negative bias voltages. At T = 40K, the peak responsivity at −7.8V was found to be 2.63 A/W at $\lambda_p$ = 10.3 μm. The $E_1$ to $E_3$ bound-to-bound (B-B) transition at T = 40K was observed for bias voltages greater than -6V. The shift of peak wavelength with applied bias for the B-B and B-C transitions is due to the quantum confined Stark effect, which were found to be about 0.4 μm (10.7 ~ 10.3 μm) and 0.3 μm (7.9 ~ 7.6 μm) between − 6V and −7.8V at T = 40K, respectively. The extrapolated peak wavelengths at zero bias voltage were found to be 9.1 μm and 12.2 μm for the $E_1$-$E_C$ and $E_1$-$E_3$ transitions, respectively. The background limited performance (BLIP) detectivity ($D^*_{BLIP}$) at $\lambda_p$ = 10.3 μm and $V_b$ = -7.8V was found to be 2.0 x $10^{10}$ cm-Hz$^{1/2}$/W at T = 40K.

### 3.4.2 The 3-Period MWIR BC-QWIP

Figure 3.6 (a), (b), (c), and (d) show the spectral responsivity of the MWIR BC-QWIP measured at different bias voltages and temperatures. The bound-to-continuum (B-C) transition was obtained for MWIR detection. At T = 77 K, the peak responsivities under negative biases were found to increase with bias voltage up to −1.3V, and the maximum peak responsivity was 0.27 A/W at $\lambda_p$ = 5.1 μm and $V_b$ = −1.3V. The peak responsivity was found to be 0.46 A/W at $\lambda_p$ = 5.1 μm, $V_b$ = 1.1V and T = 77 K. The peak wavelength at $\lambda_p$ =

5.1 μm was found to be nearly independent of the bias voltage and temperature. Figure 3.7 (a), (b), (c), and (d) show the peak responsivity versus bias voltage for the MWIR BC-QWIP measured at different temperatures. The peak responsivity at $\lambda_p = 5.1$ μm was initially increased up to the maximum value and then dropped slightly with applied bias voltage. At higher bias voltages, the photoresponse was saturated due to the large thermionic emission dark current. Figure 3.8 (a) and (b) show the peak responsivity versus temperature at (a) negative and (b) positive bias voltages, respectively. The responsivity at higher bias voltage was slightly decreased with increasing temperature. However, the responsivities at lower bias voltage were found to first increase and then decrease with increasing temperature in which the responsivity at higher biases can reach the maximum value at lower temperature. Finally, the peak detectivity and the collection quantum efficiency under background limited performance (BLIP) were found to be $D^*_{BLIP} = 1.187 \times 10^{10}$ cm-Hz$^{1/2}$/W and $\eta g = 6.5$ % at $\lambda_p = 5.1$ μm, T = 77 K, and $V_b = -1.3$V, respectively.

### 3.4.3   The Stacked-QWIP

Figure 3.9 (a) and (b) show the spectral responsivity of the MWIR and LWIR stacked-QWIP measured at different temperatures and bias voltages. The MWIR detection peak wavelengths were found to be of $\lambda_p = 5.1$ μm and were independent of bias voltage. The peak responsivity at $V_b = -9$V and $\lambda_p = 5.1$ μm was 0.2 A/W at T = 40K. The two peak detection wavelengths due to the $E_1$-$E_C$ and $E_1$-$E_3$ transitions were also observed in the LWIR region. The peak responsivity was 1.76 A/W at $V_b = -9$V, $\lambda_p = 10.3$ μm, and T = 40K. The wavelength tunability for the $E_1$-$E_3$ and $E_1$-$E_C$ transitions at T = 40K was about 0.4 μm from 10.7 μm to 10.3 μm and 0.3 μm from 7.9 μm to 7.6 μm between -7V and -9V,

respectively. The tunable peak wavelengths at T = 77K were found to be 0.2 μm varying

from 11.0 μm to 10.8 μm between −6V and −7V. The responsivity at the same bias voltage

was decreased with increasing temperature as a common result for the large period QWIPs

(more than 20 periods). The background limited performance (BLIP) detectivity (D*$_{BLIP}$) at

$\lambda_p$ = 10.3 μm was found to be 1.63 x $10^{10}$ cm-Hz$^{1/2}$/W at V$_b$ = -9V and T = 40K.

### 3.5 Conclusions

We have demonstrated a high performance high-strain two-stack, 3-color,

InGaAs/AlGaAs/InGaAs TC-QWIP and InGaAs/AlGaAs BC-QWIP for LWIR and MWIR

dual band detection. A maximum responsivity of 2.63 A/W was obtained at $\lambda_p$ = 10.3 μm,

V$_b$ = -7.8V, and T = 40K for the LWIR TC-QWIP. The strong quantum confined Stark shift

and the rapid increase of the peak responsivity with applied bias for the E$_1$-E$_3$ transition were

observed in both the LWIR TC- and stacked- QWIPs. The peak responsivity at $\lambda_p$ = 5.1 μm

due to bound-to-continuum (B-C) transition was observed up to T = 120 K for the MWIR

BC-QWIP. The peak responsivity for this device at higher bias voltages was less sensitive to

temperature while the peak responsivity at lower bias voltages was found to first increase

and then decrease with increasing temperature. The responsivity at higher bias voltages was

saturated due to the saturation of the optical gain at high bias. The peak wavelength for the

MWIR BC-QWIP was found to be at $\lambda_p$ = 5.1 μm, which was found to be independent of the

bias voltage and temperature.

Since the LWIR TC-QWIP reported here used 20 periods of QWs, a large bias voltage

(up to 9 V) was used in this device in order to obtain gain-quantum efficiency product and

high responsivity. For the low background and low bias applications, short period (3 to 5

periods) TC-QWIP structure should be used so that high peak responsivity and detectivity can be achieved in a TC-QWIP under low bias conditions.

Table 3.1. The layer structure of a high-strain multi-color, two-stack InGaAs/AlGaAs/InGaAs
TC-QWIP and InGaAs/AlGaAs BC-QWIP grown on the GaAs substrate for LWIR
and MWIR dual band detection

| Layer | | Thickness (Å) | Dopant | Concentration (cm$^{-3}$) |
|---|---|---|---|---|
| n GaAs (top contact) | | 5000 | Si | $2 \times 10^{18}$ |
| i GaAs | | 1000 | none | none |
| i Al$_{0.08}$Ga$_{0.92}$As | | 500 | none | none |
| i In$_{0.12}$Ga$_{0.88}$As | | 40 | none | none |
| i Al$_{0.08}$Ga$_{0.92}$As | | 20 | none | none |
| i In$_{0.12}$Ga$_{0.88}$As | 20-period | 40 | none | none |
| i Al$_{0.08}$Ga$_{0.92}$As | | 20 | none | none |
| n In$_{0.25}$Ga$_{0.75}$As | | 55 | Si | $7 \times 10^{17}$ |
| i Al$_{0.08}$Ga$_{0.92}$As | | 500 | none | none |
| i GaAs | | 1000 | none | none |
| i GaAs | | 5000 | Si | $2 \times 10^{18}$ |
| i Al$_{0.3}$Ga$_{0.7}$As | | 300 | none | none |
| i In$_{0.3}$Ga$_{0.7}$As | 3-period | 43 | Si | $2.5 \times 10^{18}$ |
| i Al$_{0.3}$Ga$_{0.7}$As | | 300 | none | none |
| n GaAs (bottom contact) | | 10000 | Si | $2 \times 10^{18}$ |
| S.I. GaAs substrate | | $625 \pm 25$ μm | none | none |
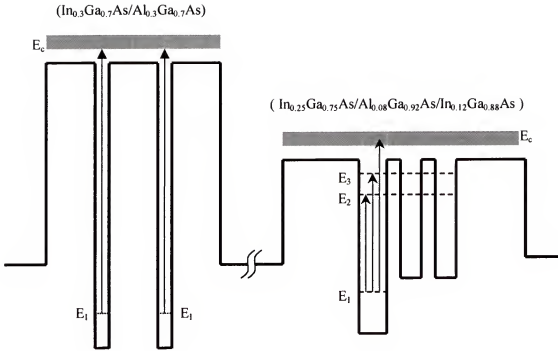
Figure 3.1. The schematic conduction band diagram of a high strain, multi-color, two-stack, InGaAs/AlGaAs/InGaAs LWIR TC- and InGaAs/AlGaAs MWIR QWIP grown on GaAs sbustrate.
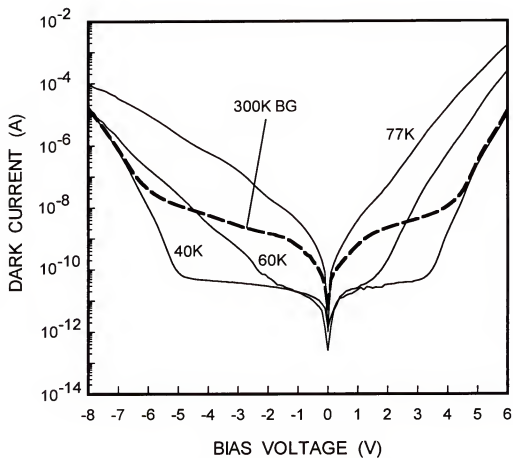
Figure 3.2. The dark current versus bias voltage (I-V) measurement at T = 40, 60, and 77K along with the 180$^\circ$ field of view (FOV) 300K background window current of the LWIR TC-QWIP
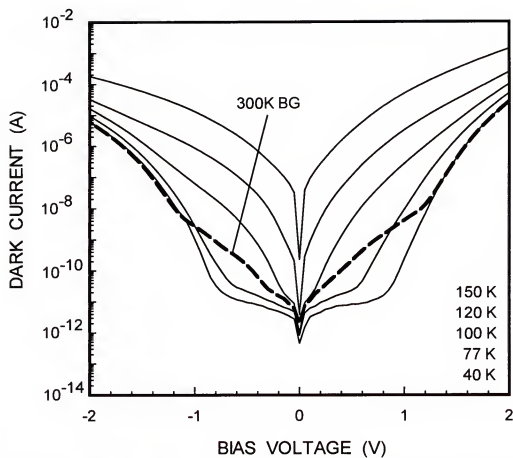
Figure 3.3. The dark current versus bias voltage (I-V) measurement at T = 40, 77, 100, 120, and 150 K along with the 180 ° field of view (FOV) 300 K background window current of the MWIR BC-QWIP
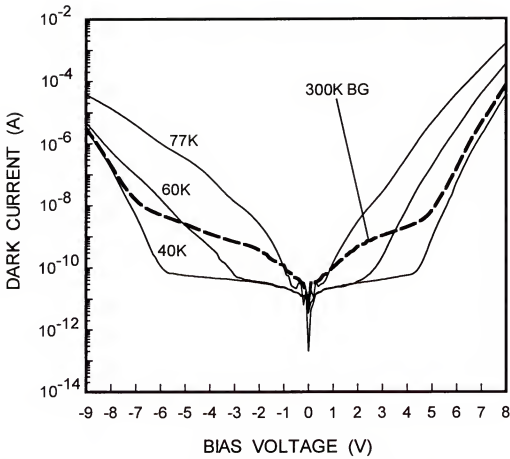
Figure 3.4. The dark current versus bias voltage (I-V) measurement at T = 40, 60, and 77 K along with the 180 ° field of view (FOV) 300 K background window current of the stacked-QWIP
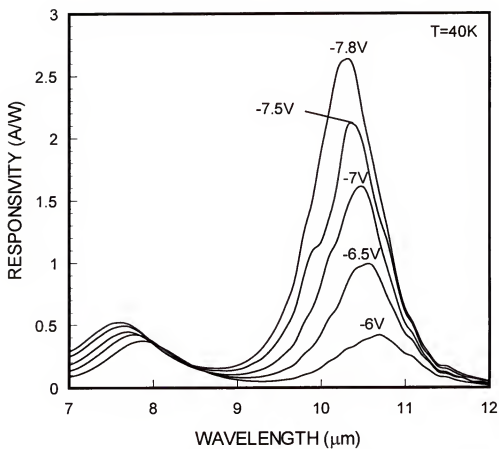
Figure 3.5. The spectral responsivity of the LWIR TC-QWIP measured at T = 40 K
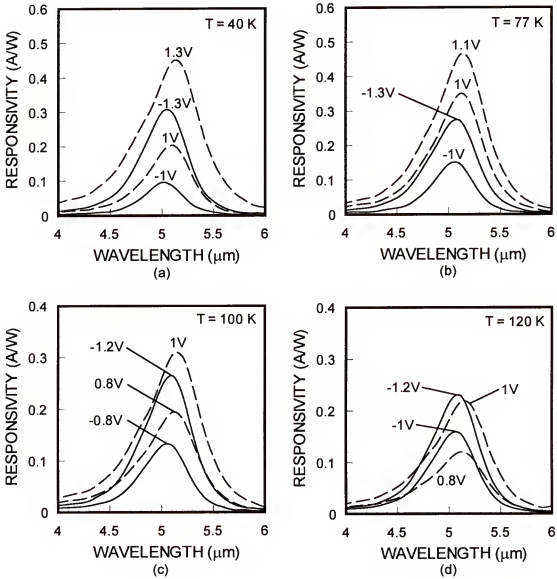
Figure 3.6. The spectral responsivity of the MWIR BC-QWIP measured at (a) 40, (b) 77, (c) 100, and (d) 120 K.
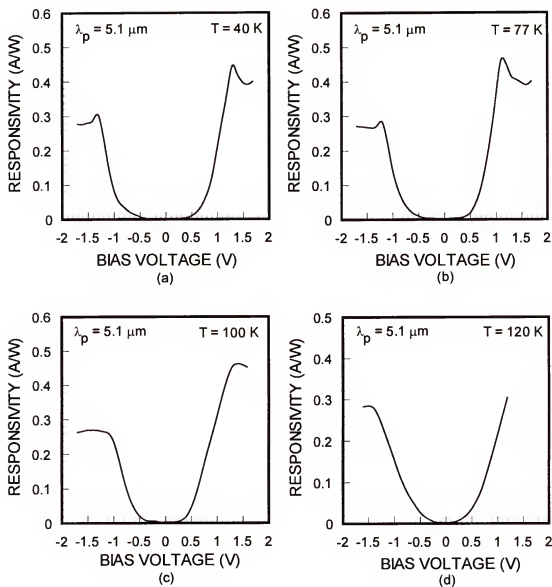
Figure 3.7. The peak responsivity at $\lambda_p = 5.1$ μm versus bias voltage for the MWIR BC-QWIP at (a) 40, (b) 77, (c) 100, and (d) 120 K.
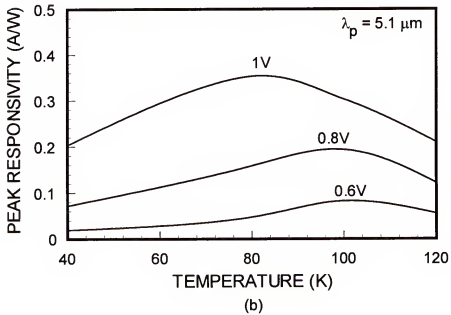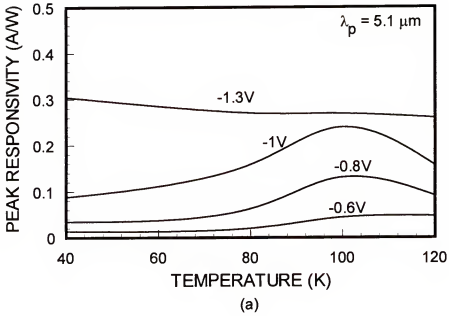
Figure 3.8. The peak responsivity versus temperature for the MWIR BC-QWIP at (a) negative and (b) positive bias voltages
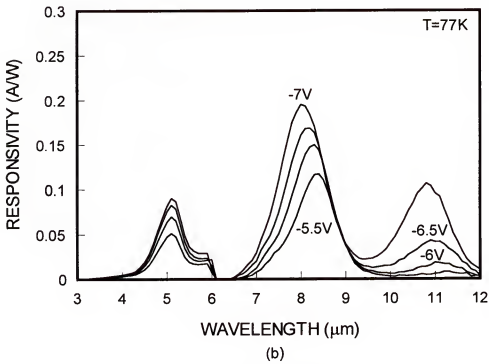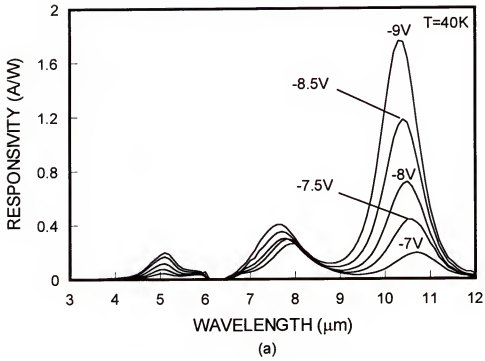
Figure 3.9. The spectral responsivity of the stacked-QWIP measured at (a) T = 40 K and (b) T = 77 K

# CHAPTER 4
## SUPERLATTICE COUPLED (SC-) QWIP FOR LONG WAVELENGTH INFRARED APPLICATION

### 4.1 Introduction

Significant progress in intersubband quantum well infrared photodetector (QWIP) technology has been made over the past decade for infrared focal plane arrays (FPAs) imaging applications [4,5]. Owing to the maturity of the III-V molecular beam epitaxy (MBE) growth and processing techniques, large format high performance single and multi-color QWIP FPAs have been demonstrated for the mid- and long-wavelength (MW/LW) infrared (IR) imaging applications [16,68]. The GaAs-based QWIP has emerged as one of the most promising photodetectors for IR imaging applications in the LWIR spectral window. The adoption of a superlattice (SL) [69] and a wide variety of asymmetrical structures such as triple-coupled (TC-) quantum well structure has helped to improve greatly the performance of the GaAs- based QWIPs. Huang and Lien [65,66] proposed a voltage-tunable two-depth three-coupled quantum well for IR detection, and Chiang *et al.* [36] reported the first voltage-tunable multicolor TC-QWIP for MWIR/LWIR detection. The TC-QWIP employs an asymmetrical triple- coupled quantum well (TCQW) structure to achieve wavelength tunability by the applied bias, with high responsivity and multicolor detection capability. In this letter we report a high performance superlattice coupled (SC)- QWIP using InGaAs/GaAs/AlGaAs material systems for LWIR detection.

## 4.2 Device Design and Processing

We designed this new QWIP structure with increasing number of six coupled wells than the TC-QWIP for improving the responsivity through stronger coupling while it has the similar features of a TC-QWIP, such as voltage tunability and multicolor detection. The SC-QWIP uses 5 periods of the unit cells each formed by a 300 Å thick barrier layer and 6 superlattice- coupled (SC) wells which consist of one 84 Å $In_{0.22}Ga_{0.78}As$ deep well (Si-doped to $N_d = 7 \times 10^{17}$ $cm^{-3}$) and 5 superlattices formed by a 55 Å undoped GaAs shallow well and a 70 Å $Al_{0.09}Ga_{0.91}As$ barrier. An undoped GaAs spacer layer with thickness of 1000 Å and an ohmic contact layer ($N_d = 2 \times 10^{18}$ $cm^{-3}$) with a thickness of 5000 Å were grown on both sides of the active layers of the SC- QWIP. This SC-QWIP structure was grown on the semi-insulating (SI) GaAs substrate by using the molecular beam epitaxy (MBE) technique.

To characterize the device, a $200 \times 200$ $\mu m^2$ mesa structure was formed on the GaAs wafer using standard photolithography and wet chemical etching processes. Alloy of AuGe/Ag/Au films were deposited by E-beam evaporation to form the top and bottom ohmic contacts. Finally, a 45° facet was polished on the substrate for coupling the incident IR radiation into the quantum wells.

Figure 4.1 (a) shows the schematic conduction band diagram and the intersubband transition scheme for the SC-QWIP and Figure 4.1 (b) shows the whole QWIP structure of the processed device. As can be seen in Fig. 4.1 (a) a global miniband is formed in the deep-well and the superlattice coupled wells of the SC- QWIP. Due to the strong coupling of the deep- well and the superlattice wells, the bound states ($E_{SL}$) in the GaAs/AlGaAs superlattices and the first excited state ($E_2$) in the InGaAs QW are coupled to form a global

miniband [69] inside the SC-QWs, as illustrated in Fig. 4.1 (a). Under positive bias condition the photo-excited carriers can be easily tunneling through the miniband due to barrier lowering, but under negative bias condition the photo-excited carriers can tunnel through the thick barrier only under high bias condition. As a result, the spectral responsivity is expected to be higher under positive bias (+$V_b$) than under negative bias (-$V_b$) condition.

## 4.3 Results and Discussion

### 4.3.1 Responsivity

The absolute spectral responsivity ($R_i$) can be expressed in terms of the quantum efficiency ($\eta$) and photoconductive gain ($g$) as [70]

$$R_i = \frac{q\lambda\eta}{hc}g = \frac{q}{h\nu}\eta_c = \frac{\lambda}{1.24}\eta g, \tag{4.1}$$

where $q$ is the electronic charge, $\lambda$ is the wavelength of the incident photon, $h$ is the Planck constant, $c$ is the speed of light, $\nu$ is the incident frequency, and $\eta_c$ is the collection efficiency ($\eta g$), which is the product of quantum efficiency ($\eta$) and photoconductive gain ($g$). The spectral responsivity can also be calculated by using the expression given by

$$R_i = \frac{I_p}{P_{in}}, \tag{4.2}$$

where $I_p$ is the photocurrent output (A) converted by a transimpedance amplifier (TIA) and measured by a lock-in amplifier, and $P_{in}$ is the input IR radiation power (W) obtained using a calibrated pyroelectric detector.

The transmission coefficient calculated by using the transfer matrix method (TMM) is shown in the inset of Fig. 4.1 (a), which clearly shows the formation of miniband by the superlattice coupled wells. The calculated peak detection wavelength for this SC-QWIP was

10.4µm, which was found in excellent agreement with the measured value (10.5µm). The photocurrent spectra were measured by 45° facet backside illumination using a monochromater, a calibrated blackbody-source, and a cryogenic system. The spectral responsivities measured at T = 20K and 40K under positive and negative bias conditions are shown in Figure 4.2 (a), (b). The photoresponse was dominated by the $E_1$ to $E_{SL}$ miniband states transition, and the maximum responsivity at $\lambda_p = 10.5$ µm under positive bias is 4.95 A/W at $V_b = 3.15V$ and T = 20K. The maximum responsivity under negative bias at $\lambda_p = 10.7$ µm is 2.05 A/W at $V_b = -3.6V$ and T = 20K. A maximum responsivity of R = 3.64 A/W was obtained at $\lambda_p = 10.5$ µm, $V_b = 3.15V$ and T = 40K., and R = 1.86 A/W at $\lambda_p = 10.7$ µm and $V_b = -3.6V$. The large responsivity value of 3.64 A/W obtained at 40K is significantly improved over those TC-QWIPs reported earlier [36,67] and other QWIPs with different structures. The Stark shift effect [66] was not observed in this device under positive bias condition. However, a small red- shift of the peak wavelength with applied bias was observed under negative bias condition (i.e., $\lambda_p$ shifts from 10.5 µm to 10.7 µm as $V_b$ varies from –2V to –3.6V at 20K). The results reveal that the wavelength tunability for this SC-QWIP is much smaller than the TC-QWIP reported earlier by our group [36]. The weak Stark shift effect may be attributed to the formation of miniband in the SC-QWIP, which has a much smaller energy shift than the single bound state by the applied bias. The full-width half-maximum (FWHM) spectral bandwidth of this device at $V_b = -3.6V$ was found to be $\Delta\lambda/\lambda_p = 9.35\%$, while FWHM spectral bandwidth at $V_b = 3.15V$ was found to be $\Delta\lambda/\lambda_p = 9.5\%$. These narrow responsivity bandwidths are similar to the previously reported bound-to-miniband transition QWIPs [50]. The bias dependent responsivity was measured for the 10.4 µm response peak at 40K, and the result is shown in Figure 4.3. As can be seen from

this figure, the responsivity remains zero at low biases and increases rapidly from zero to −2.7V for negative biases and zero to +1.8V for positive biases, which shows the characteristics of an asymmetrical QWIP.

### 4.3.2 Dark Current and Thermal Activation Energy

The dark current-voltage (I-V) curves measured at different temperatures are shown in Fig. 4.4 for the SC-QWIP. The I-V characteristics are asymmetrical since the effective barrier height under positive bias is smaller than under negative bias condition for the thermionic emission dark current. The device was found under the background limited performance (BLIP) condition for $-2.8V < V_b < 2.6V$ at 20K, and $-1.9V < V_b < 2.1V$ at 40K, respectively.

The thermal activation energy ($E_{ac}$) due to thermionic emission can be determined from the dark currents (Fig. 4.4) using the Arrhenius plot. Figure 4.5 (a) shows the normalized dark current ($I_d$/T) versus the normalized inverse temperature (1000/T) at different biases, and Figure 4.5 (b) shows the thermal activation energy ($E_{ac}$) versus the applied bias voltage at 40K for the SC-QWIP. By extrapolating the experimental curve the activation energy at $V_b = 0V$ was found to be $E_{ac} = 84.5$ meV. The cutoff energy $E_c$ ($E_b$-$E_1$ = 108.7 meV) and the Fermi energy ($E_F = 24.2$ meV) were obtained from the transfer matrix method (TMM) and the relevant equations. The calculated cutoff wavelength was $\lambda_c = 11.4$ μm, which is in excellent agreement with the measured value of $\lambda_c = 11.2$ μm. As shown in this figure, the activation energy was decreased with increasing bias voltage due to the electron tunneling conduction through the barriers at high biases.

### 4.3.3 Spectral Detectivity

The spectral detectivity ($D^*$) can be obtained from the noise gain $g$ (V) and the measured dark current and responsivity of device. The noise gain is given by [71]

$$g(V) = \frac{I_d R_0}{\frac{kT}{q} N^2 \exp(\frac{\Delta E}{kT})} \, , \tag{4.3}$$

where $R_0$ is the dynamic resistance at zero bias, $N$ is the number of periods, $k$ is the Boltzmann constant, $\Delta E$ is the barrier lowering, which is given by

$$\Delta E = q\sqrt{\frac{qV_b}{4l_t \pi \varepsilon_0 \varepsilon_r}} \, , \tag{4.4}$$

where $V_b$ is the bias voltage across one period, $l_t$ is the length of one period, $\varepsilon_0$ is the free space permittivity, and $\varepsilon_r$ is the dielectric constant. The detectivity can be calculated from

$$D_\lambda^* = R_i\sqrt{\frac{A_d \Delta f}{4qI_d g}} \, , \tag{4.5}$$

where $R_i$ is the responsivity, $A_d$ is the device area, $\Delta f$ is the band width, $q$ is the electron charge, and $I_d$ is the dark current. Values of $D^*$ for the SC-QWIP at $\lambda_p$ = 10.5 μm were calculated using Eqs. (4.3) - (4.5), which yield $D^*$ = 1.83 x $10^{10}$ and 1.68 x $10^{10}$ cm-Hz$^{1/2}$/W at $V_b$ = 3.15V, T = 20 K and at $V_b$ = 3V, T = 40 K, respectively.

### 4.4 Conclusions

In summary, a high sensitivity superlattice- coupled (SC)- InGaAs/GaAs/AlGaAs QWIP, which uses an SC - quantum wells and exhibits a peak detection wavelength at 10.5 μm, has been demonstrated in this work. Excellent responsivity and detectivity due to the use of SC - quantum wells have been obtained and analyzed for this QWIP device. The

maximum responsivity and peak detectivity ($D^*$) at $\lambda_p$ = 10.5 $\mu$m and T = 20K under positive bias were found to be $R_i$ = 4.95 A/W and $D^*$ = 1.83 x $10^{10}$ cm-Hz$^{1/2}$/W at $V_b$ = 3.15V, respectively. Further refinement can be made on this structure to tailor the peak wavelength and to improve the responsivity by altering the material composition, layer thickness, and the number of superlattice- coupled quantum wells.

(a)



(b)
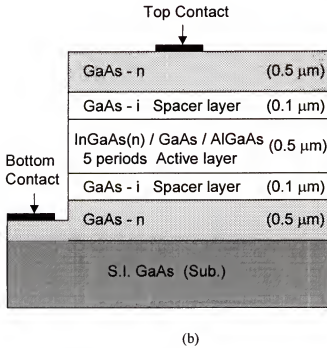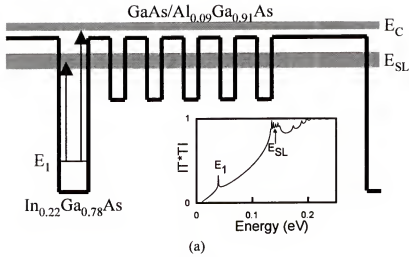
Figure 4.1. (a) Schematic conduction band diagram and the transition scheme for the AlGaAs/GaAs/InGaAs superlattice coupled (SC)- QWIP. The inset shows the calculated transmission coefficient versus energy level using TMM.
(b) Schematic diagram of the processed device.
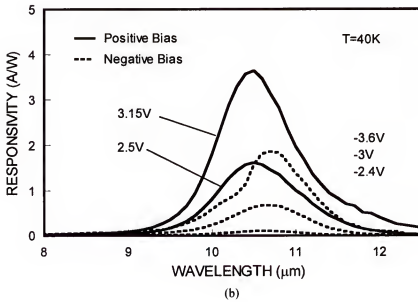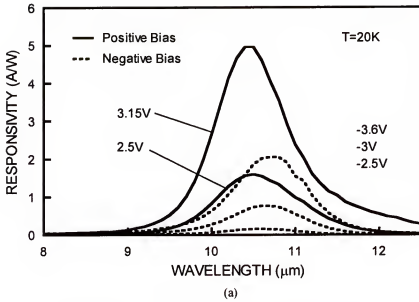
Figure 4.2. Responsivity versus wavelength for the SC-QWIP at (a) T = 20K and (b) T = 40K.
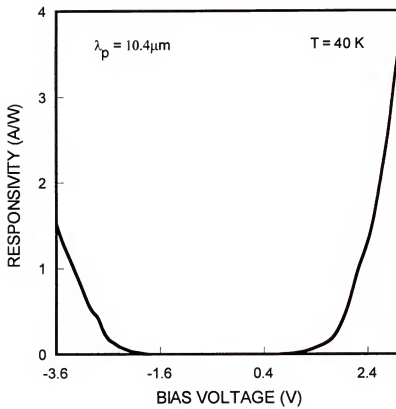
Figure 4.3. Responsivity versus bias voltage for the SC-QWIP at $\lambda_p$ = 10.4 μm and 40K.
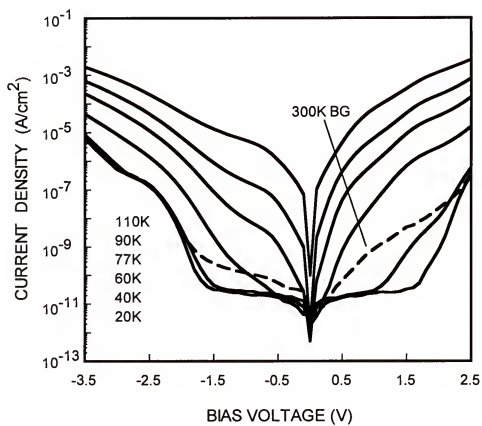
Figure 4.4. Dark current-voltage (*I-V*) characteristics for the SC-QWIP.
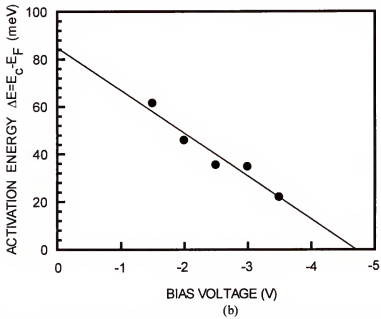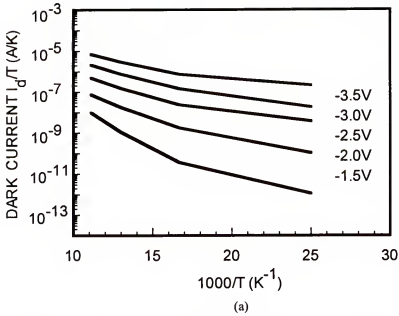
Figure 4.5. (a) The normalized dark current versus the inverse temperature for the SC-QWIP, and (b) activation energy versus bias voltage for the SC-QWIP.

CHAPTER 5
THEORETICAL CONSIDERATIONS OF TYPE II INFRARED PHOTODETECTOR FOR
LONG- AND VERY LONG-WAVELENGTH DETECTION

## 5.1 Introduction

Since infrared detectors in the mid and long wavelength spectral region (3-14um) have many medical, industrial, and military applications, a substantial effort has been devoted in recent years to the development of large focal plane arrays (FPA) of photovoltaic, photoconductive detectors sensitive to infrared (IR) radiation in this range and beyond [72,73]. However, in most of the applications, cryogenic coolers are not desirable because of their short lifetime and the added power consumption weight, volume, and cost. Commercially available infrared detectors in this wavelength range can be categorized as interband, which are HgCdTe and InAsSb, or intersubband quantum-well infrared detectors (QWIPs). Unfortunately, there are some fundamental problems, namely the fast Auger recombination in interband detectors and the high thermal generation rate in intersubband detectors, which drastically decrease their ability for near room temperature operation in this infrared range.

GaSb based IR detector using type II superlattices structure has been proposed as another alternative for infrared photodetectors in this spectral range. In comparison to HgCdTe, the higher effective mass of electrons and holes and the slower Auger recombination rate lead to lower dark current and higher operating temperature in type II superlattices IR detector scheme. Another advantage of a type II superlattice is the possibility of band-gap engineering. Unlike bulk material or type I superlattices as shown in

Figure 5.1, one can modify the energy of the conduction and valence minibands of a type II superlattice with a high degree of freedom. To obtain a good optical response from the superlattice, it is necessary to have a large overlap between the electron and hole wavefunction. However, since in type II superlattices the electrons and holes are confined to different materials, the layers of each material must be kept thin enough to allow this overlap to occur. For InAs/GaSb structures the required wavelengths can only be achieved by using thick layers, to reduce the quantum confinement effect. Alloying InSb or AlSb into the GaSb (InAs/GaInSb or InAs/AlGaSb) increases the well overlap allowing the required energy gaps to be achieved with thinner layers.

### 5.2 Type II IR Detector based on InAs/GaInSb Strained Layer Superlattices

Figure 5.1 shows schematic illustration of the band line-ups of type I and type II superlattices at a semiconductor interface. Promising InAs/GaInSb IR detectors have a broken type II band structure and the valence band splitting caused by strained layers as shown in Figure 5.1 (c) and Fig. 5.2 (b), respectively. This unique band structure gives this detector some prominent advantages over commercially available IR detectors like MCT detectors and QWIPs in long-wavelength and very long-wavelength spectral regimes. In addition, due to their broken band gap alignment the superlattice band gap of type II detectors can be smaller than that of either of the constituent materials and it gives a higher degree of band gap engineering up to very long-wavelength IR region.

MCT detectors and QWIPs have some essential problems such as the high Auger recombination rates and the large tunneling dark current in HgCdTe and the high thermal generation rate in QWIPs and these problems cause to decrease drastically their performance

at near room temperature in longer wavelength IR range. The electronic band structure of InAs/GaInSb superlattices, which differs qualitatively from that of bulk zincblende materials, solves these problems while suppressing the Auger recombination and tunneling rates. The heavy- and light- hole splitting results in large imaginary wave vectors for states in the superlattice gap, reducing the probability of tunneling and hence the noise associated with this leakage mechanism. Furthermore, designing a detector structure to have a mini-gap between the superlattice subbands one energy band gap below the valence band edge suppresses the Auger processes for which the in-plane wave vector is small (i.e., $k_\parallel \approx 0$). Conservation of energy and momentum requires that an electron recombines with a hole having a sizable in-plane wave vector, but dispersion in $k_\parallel$ makes such a state unlikely to be occupied by a hole at low temperatures. Auger processes often dominate radiative processes in MCT, whereas the opposite is often true in the type-II InAs/GaInSb superlattice IR detector.

Interests in IR detectors based on type II InAs/GaInSb superlattices are motivated by the calculated performance superior to those of conventional technology based on bulk HgCdTe [73-77]. Significant improvements in the optical quality of there superlattices have been expected [75] and room temperature operation has been demonstrated for this material system [72]. Unlike in the case of HgCdTe, p-type absorbing layers are desirable in the superlattice IR detector, for reason of both transport and carrier lifetime. Although Auger process can be suppressed in n-type superlattice, the effect is usually greater in p-type structures [78]. The doping density of $10^{17}$ cm$^{-3}$ is optimized for p-type superlattice [78] and an undoped layer was inserted between p-n interface to lower the tunneling current by reducing band bending at the heterojunction.

### 5.3 $k \cdot p$ Theory for InAs/GaInSb Superlattice Band Structure

The InAs/GaInSb superlattice band structure can be obtained from a second-order 8 x 8 $k \cdot p$ formulation as described by Kane [79] and Pikus and Bir [80]. In the eight-band description of the electronic structure of bulk materials, it is assumed that the band structure can be well described by a $k \cdot p$ Hamiltonian at the center of the Brillouin zone by including the $J = 3/2$ heavy-hole (HH) and light-hole (LH) bands, and the $J = 1/2$ spin orbit split-off valence bands together with the $\Gamma_6$ conduction bands. The Hamiltonian is expanded to first order in the strain tensor and it goes beyond the usual Pollak and Cardona [81] approximation to appropriately include the effects of strain on states other than k = 0. The model also considers the effect of strain on the spin-orbit coupling. The Luttinger parameters and the momentum matrix elements for each layer are calculated from its bulk band gap electron, LH, HH, and split-off masses [82,83]. A simple linear average is employed for the ternary compound. The superlattice band structure is obtained by transforming the bulk 8 x 8 $k \cdot p$ Hamiltonian into a set of eight coupled second-order differential equations by finite difference technique. An important advantage of this approach over others is that the problem is reduced to a single eigenvalue equation of the form $\mathbf{H} \cdot \mathbf{F} = E\mathbf{F}$, wherein the complex Hermitian matrix $\mathbf{H}$ can be diagonalzed by standard techniques to obtain both the eigenvalues $E$ and eigenvectors $\mathbf{F}$. The linear absorption coefficient, apart from a constant factor, between the two superlattice energy states $E_n$ and $E_{n'}$ can be calculated [83] using:

$$\alpha(\hbar\omega) = \frac{1}{\hbar\omega} \sum_{nn'} \int d^3k \; |M_{nn'}(k_{\parallel},q)|^2 \; \delta[E_n(k_{\parallel},q) - E_n(k_{\parallel},q) - \hbar\omega], \qquad (5.1)$$

where $\hbar\omega$ is the photon energy and $M_{nn'}$ is the optical matrix element between the $n$th and $n'$th states. The term $k_{\parallel}$ is the component of the total superlattice wavevector $k$ in the in-plane direction and $q$ is the component of $k$ along the growth direction. Since the electron-

hole Coulomb interaction (excitonic effect) in type II superlattices is expected to be much weaker as compared with type I GaAs/AlGaAs superlattices, this effect is not included in Eq. (5.1).

## 5.4 Strained Layer Superlattices

The lattice-mismatch induced strains in the constituent materials forming the superlattice are calculated by minimizing the strain energy subject to the constraints imposed by the pseudomorphic character of the interfaces. We define the set of orthonormal vectors $\{\hat{\mathbf{n}}_i\}$ so that $\hat{\mathbf{n}}_1$ and $\hat{\mathbf{n}}_2$ lie in the superlattice plane and $\hat{\mathbf{n}}_3$ is orthogonal to this plane. We define the vectors

$$\begin{bmatrix} \mathbf{x}_i \\ \mathbf{y}_i \\ \mathbf{z}_i \end{bmatrix} = \begin{bmatrix} (1 + \varepsilon_{xx}^i) & \varepsilon_{xy}^i & \varepsilon_{xz}^i \\ \varepsilon_{yx}^i & (1 + \varepsilon_{yy}^i) & \varepsilon_{yz}^i \\ \varepsilon_{zx}^i & \varepsilon_{zy}^i & (1 + \varepsilon_{zz}^i) \end{bmatrix} \begin{bmatrix} \hat{\mathbf{x}} \\ \hat{\mathbf{y}} \\ \hat{\mathbf{z}} \end{bmatrix}, \tag{5.2}$$

where $i$ labels the two constituent materials of the superlattice. The off-diagonal strain components are diagonal ($\varepsilon_{ij} = \varepsilon_{ji}$), so that six unknown strain components are to be determined in each of the two constituent materials. Without loss of generality, we consider a superlattice grown from two zinc-blende structure compound semiconductors. The zinc-blende structure primitive lattice translation vectors are

$$\mathbf{a}_i = \frac{a_i}{2}(\hat{\mathbf{y}} + \hat{\mathbf{z}})$$

$$\mathbf{b}_i = \frac{a_i}{2}(\hat{\mathbf{z}} + \hat{\mathbf{x}}), \tag{5.3}$$

$$\mathbf{c}_i = \frac{a_i}{2}(\hat{\mathbf{x}} + \hat{\mathbf{y}})$$

where $a$ is the length of the cube edge. When the crystal is strained, the primitive translation vectors become

$$\mathbf{a'}_i = \frac{a_i}{2}(\mathbf{y}_i + \mathbf{z}_i)$$
$$\mathbf{b'}_i = \frac{a_i}{2}(\mathbf{z}_i + \mathbf{x}_i). \tag{5.4}$$
$$\mathbf{c'}_i = \frac{a_i}{2}(\mathbf{x}_i + \mathbf{y}_i)$$

The conditions for pseudomorphic interface are

$$\mathbf{a'}_i \cdot \hat{\mathbf{n}}_1 = \mathbf{a'}_j \cdot \hat{\mathbf{n}}_1, \quad \mathbf{a'}_i \cdot \hat{\mathbf{n}}_2 = \mathbf{a'}_j \cdot \hat{\mathbf{n}}_2$$
$$\mathbf{b'}_i \cdot \hat{\mathbf{n}}_1 = \mathbf{b'}_j \cdot \hat{\mathbf{n}}_1, \quad \mathbf{b'}_i \cdot \hat{\mathbf{n}}_2 = \mathbf{b'}_j \cdot \hat{\mathbf{n}}_2 . \tag{5.5}$$
$$\mathbf{c'}_i \cdot \hat{\mathbf{n}}_1 = \mathbf{c'}_j \cdot \hat{\mathbf{n}}_1, \quad \mathbf{c'}_i \cdot \hat{\mathbf{n}}_2 = \mathbf{c'}_j \cdot \hat{\mathbf{n}}_2$$

These constraint conditions are linearized in the lattice constant difference, $\Delta a_0 = a_0{}^{(a)} - a_0{}^{(b)}$. The constraint equations reduce the number of unknowns (from 12 to 7), which are determined by minimizing the superlattice strain energy density. The strain energy density of a zinc-blende structure material is

$$U_i = \frac{1}{2}c_{11}[(\varepsilon_{xx}^i)^2 + (\varepsilon_{yy}^i)^2 + (\varepsilon_{zz}^i)^2] + 2c_{44}^i[(\varepsilon_{xy}^i)^2 + (\varepsilon_{yz}^i)^2 + (\varepsilon_{zx}^i)^2]$$
$$+ c_{12}^i[\varepsilon_{yy}^i \varepsilon_{zz}^i + \varepsilon_{xx}^i \varepsilon_{zz}^i + \varepsilon_{xx}^i \varepsilon_{yy}^i] \tag{5.6}$$

where the coefficients $c_{11}$, $c_{12}$, and $c_{44}$ are the elastic constants. For a strained layer superlattice synthesized from two zinc-blende structure materials, the strain energy density is

$$U_{ab} = \frac{U_a h_a + U_b h_b}{h_a + h_b}, \tag{5.7}$$

where $h_a$ ($h_b$) is the layer thickness of material a (b). The strain components in the constituent materials are determined by minimizing the strain energy density $U_{ab}$ subject to the pseudomorphic constraints, Eq. (5.5). For a superlattice grown along the (0 0 1) axis

from two zinc-blende structure materials, only diagonal strain components are generated (e.g., $\varepsilon_{xy} = 0$) by the lattice mismatch. The diagonal components are given by [84]

$$\varepsilon_{zz}^{i} = -\left(\frac{2c_{12}^{i}}{c_{11}^{i}}\right)\varepsilon_{xx}^{i}$$

$$\varepsilon_{xx}^{a} = \varepsilon_{yy}^{a} = -\left(\frac{\Delta a_0}{a_0}\right)\left(\frac{G^b h_b}{G^a h_a + G^b h_b}\right),$$

$$\varepsilon_{xx}^{a} = \varepsilon_{yy}^{a} = \left(\frac{\Delta a_0}{a_0}\right)\left(\frac{G^a h_a}{G^a h_a + G^b h_b}\right) \tag{5.8}$$

where

$$\Delta a_0 = a_0^{(a)} - a_0^{(b)}$$

$$a_0 \frac{1}{2}\left[a_0^{(a)} + a_0^{(b)}\right] \qquad . \tag{5.9}$$

$$G^i = 2\left[c_{11}^{i} + c_{12}^{i} - \frac{2(c_{12}^{i})^2}{c_{11}^{i}}\right]$$

Neglecting the spin dependence of the stress interactions, the strain Hamiltonian for a (0 0 1)-oriented strained layer superlattice is independent of spin and has nonzero matrix elements [85]:

$$\langle s|H_{strain}^{i}|s\rangle = c^i(2\varepsilon_{xx}^{i} + \varepsilon_{zz}^{i})$$

$$\langle x|H_{strain}^{i}|x\rangle = \langle y|H_{strain}^{i}|y\rangle = (l^i + m^i)\varepsilon_{xx}^{i} + m^i\varepsilon_{zz}^{i}, \tag{5.10}$$

$$\langle z|H_{strain}^{i}|z\rangle = 2m^i\varepsilon_{xx}^{i} + l^i\varepsilon_{zz}^{i}$$

where, c, l, and m are deformation-potential constants. In Eqs. (5.10), the valence-band functions $|x\rangle, |y\rangle$, and $|z\rangle$ belong to the irreducible representation $\Gamma_{15}^{v}$ and the conduction-band function $|s\rangle$ belong to the irreducible representation $\Gamma_{1}^{c}$.

## 5.5 Type II IR Detector Figures of Merit

The figures of merit for a type II IR detector are similar to that of QWIPs including dark current, responsivity, and detectivity. Under conditions where the noise is dominated by generation and recombination processes, the noise current is given by [86]

$$I_n = e\sqrt{2d(G+R)A\Delta f},$$ (5.11)

where $G$ and $R$ are the carrier generation and recombination rates, respectively, $A$ is the detector area, $\Delta f$ is the bandwidth, and $d$ is the detector thickness. The responsivity for photons of energy, $h\nu$, is defined as

$$R = \frac{I_{ph}}{P_I} = \frac{I_{ph}}{\Phi A h\nu},$$ (5.12)

where $I_{ph}$ is the photocurrent, $P_I$ is the incident power, and $\Phi$ is the photon flux. If $\eta$ electron-hole pairs are produced and contribute to $I_{ph}$ for each incident photon and assuming unity photoelectric gain, then $I_{ph} = \eta\, e\, \Phi A$, and the responsivity $R$ is

$$R = \frac{\eta e}{h\nu}.$$ (5.13)

The photoconductor detectivity is calculated following the assumptions of Kinch and Borrello [87] and Piotrowski *et al.* [88] and given by

$$D^* = R\frac{\sqrt{A\Delta f}}{I_n},$$ (5.14)

where $I_n$ is the noise current. Employing (5.11) and (5.13) in (5.14) gives the device detectivity

$$D^* = \frac{\eta}{h\nu}\frac{1}{\sqrt{2d(G+R)}}.$$ (5.15)

For the photodiode, the detectivity is given by [89]

$$D^* = R\sqrt{\frac{R_0 A}{4kT}}, \tag{5.16}$$

where $T$ is the operation temperature in degrees Kelvin and $R_0$ is the zero-bias differential resistance.
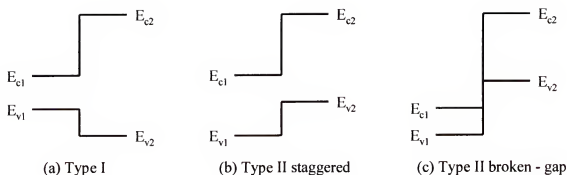
Figure 5.1  Band line-ups of Type I, Type II at semiconductor interfaces
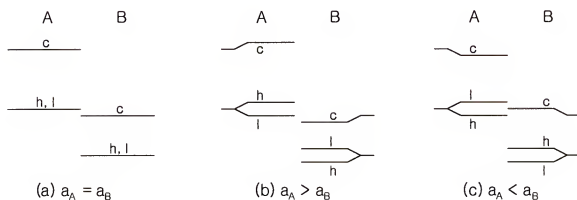


Figure 5.2 Schematic diagram of the band-edge lineup in type II superlattices for three strain conditions (for lattice constants of materials A and B, $a_A$, $a_B$)

CHAPTER 6

SIMULATION OF AN InAs/GaInSb TYPE II SUPERLATTICE INFRARED
PHOTODETECTOR FOR LONG- AND VERY LONG-WAVELENGTH DETECTION

### 6.1 Introduction

Development of GaInSb strained layer superlattices has largely been motivated by the promise of overcoming fundamental and practical limitations of conventional, high performance infrared (IR) detectors such as those based on HgCdTe (MCT) and quantum-well infrared photodetectors (QWIPs). A mature superlattice technology could ease detector cooling requirements or give higher performance at a fixed operating temperature, and could demonstrate both uniformity and producibility superior to that of other intrinsic IR detectors. While these advantages are more pronounced at longer wavelengths, they appear to hold for a wide range of cutoff wavelengths. $InAs/Ga_{1-x}In_xSb$ superlattice IR detectors could cover the 3-20 μm spectral range, which include the long-wavelength infrared (LWIR) and very long-wavelength infrared (VLWIR) spectral windows. In contrast to MCT and QWIPs, the higher electron effective mass and the slower Auger recombination rate are the two main advantages of the type-II superlattice detectors for lower dark current and higher detectivity. In addition, energy gaps are subject to the selection of the superlattice thickness rather than that of the compositions, resulting in an improved uniformity across the wafer.

The staggered band offsets of the type-II superlattice (SL) based on III-V materials allow the fabrication of the intrinsic LWIR/VLWIR superlattice IR detectors, which extends the III-V growth and processing technologies to the wavelength range not available for bulk III-V materials [75]. Recently, type-II SL IR detectors using InAs/GaSb

material system have been successfully demonstrated [28,90,91]. However, the thick layer of InAs/GaSb superlattice, required for LWIR or VLWIR detection, prohibits this superlattice to achieve sufficient large optical matrix elements to be useful for LWIR or VLWIR detector applications since in superlattice structure the optical matrix elements tend to decrease rapidly with increasing layer thickness [92]. In contrast, InAs/GaInSb material system employs the lattice mismatch to create splitting of the zone center valence bands into the heavy- and light- hole components. The presence of coherent strain from this lattice mismatch is beneficial because the band edges shift in such a way that the SL energy gap is reduced without increasing the super lattice layer thickness [75]. Consequently, the small band gap superlattice can be obtained with sufficiently thin superlattice layers for large absorption coefficients. It was also reported that the Auger recombination could be successfully suppressed by the valence band splitting caused by this lattice mismatch in the p-type GaInSb/InAs superlattice for LWIR detection [25]. Large splitting between the first heavy- and light-hole valence bands impedes the hole-hole scattering Auger process, which results in improving the Auger limited minority carrier lifetimes, detectivity, and the background limited performance (BLIP) temperature [25]. Therefore, the InAs/GaInSb material system is more attractive in achieving high performance IR detectors than the InAs/GaSb system for LWIR/VLWIR applications.

In this chapter, we have theoretically investigated the composition and layer thickness of InAs/GaInSb superlattice for designing optimal LWIR/VLWIR detectors with large absorption coefficient and high detectivity. The transfer matrix method (TMM) based on the eight-band $k \cdot p$ model was employed to calculate the energy band gaps and valence band splitting [93]. In this calculation, we used 0.51 eV as the value of valence band offset

[25] and assumed that the valence band offset does not change with the increment of InSb mole fraction in the GaInSb alloys [74]. Based on these simulations, we propose several detector designs, which may be used in the future work.

## 6.2 Calculation of Critical Thickness

In order to grow the strain structure without misfit dislocations, the layer thickness cannot be more than a certain threshold, which is called critical thickness. If the layer thickness exceeds the critical thickness, misfit dislocations are created in the structure. If the creation of dislocations is confined only on the interface plane, then $h_c$ can be expressed by [94]

$$h_c = \frac{b}{8\pi(1+\gamma)f}\left[\ln(\frac{h_c}{b})+1\right], \tag{6.1}$$

where $\gamma = C_{12}/(C_1+C_2)$ is the Poisson's ratio, $f=|a_s - a_l|/a_s$ is the misfit, and in many (1 0 0) semiconductor systems $b$ is given by $a/\sqrt{2}$. For the case, which the interface place is not the only plane the dislocations can be formed, the formula is given by Matthew as like [96]

$$h_c = \frac{b(1-\gamma\cos^2\theta_{db})}{8\pi(1+\gamma)f\cos\lambda}\left[\ln(\frac{h_c}{b})+1\right]. \tag{6.2}$$

Eq. (6.2) reduces to Eq. (6.1), if $\lambda = 0°$ and $\theta_{db} = 90°$. From Eqs. (6.1) and (6.2), the critical thickness of InAs and GaInSb layers grown on the GaSb substrate was calculated. In the calculation, we assumed (1 0 0) substrate, $b = a/\sqrt{2}$ and $\theta_{db} = \lambda = 60°$. In the case of InAs layers, the critical thickness was found to be 80.28 Å by Eq. (6.1) and 175.56 Å by Eq. (6.2). The critical thickness of GaInSb layers changed with the increment of InSb mole fraction is shown in Figure 6.1. In this figure, the solid line denotes the case that the misfit dislocation

is formed at the interface while the dotted line is for the case in which the dislocation is not inhibited to lie on the interface. Since beyond the critical thickness by Eq. (6.2) the dislocation might be produced inside the bulk InAs or GaInSb layers as well as on the interface between the InAs and GaInSb layer, the degradation of type-II superlattice IR detectors could be more severe than that of the case in which the critical thickness is limited by Eq. (6.1). For this reason, the GaInSb layer thickness required for detection of specified wavelengths (9-17μm) should not exceed the limit shown by the dotted line in Figure 6.1, and the InAs thickness should also be limited to less than 175.56 Å, as given by Eq. (6.2).

### 6.3 Optimization of InAs/GaInSb Superlattice

The key criteria and optimization procedures for the design of InAs/GaInSb superlattice IR detectors with large absorption coefficient and high detectivity are summarized as follows:

(1) To minimize the Auger recombination rate, splitting between the heavy- and light-hole valence bands should be maximized. This can be achieved by increasing the thickness ratio of the constituent layers and the mole fraction of InSb in the GaInSb alloy.

(2) To maximize the absorption coefficients, thinner superlattice layer is desirable and hence higher InSb mole fraction and higher thickness ratio are needed.

(3) While the InSb composition ratio should be high for achieving high detectivity and large absorption coefficients, high InSb composition ratio corresponds to large lattice mismatch, which would cause severe strain in the superlattice, resulting in poor superlattice structure. Therefore, the InSb alloy composition should be

minimized for the defect-free superlattice structure and the exact controlling of detection wavelength, which requires to compromise with the criteria that the InSb composition must be maximized for high valence band splitting and thin constituent layers.

(4) The GaSb substrate is more advantageous in reducing the threading of misfit dislocation in the superlattice than the GaAs substrate [74] since there is no dislocation sources such as the large lattice mismatch at the GaAs-GaSb interface fro the GaAs substrate. However, it has been reported recently that the compliant GaAs substrate is best for achieving high photoresponse without the dislocation problem by using thick GaSb buffer layer grown on GaAs substrate while getting high IR transmission through GaAs [95].

(5) If the average lattice constant of the superlattice is equal to the lattice constant of the GaSb substrate or GaSb buffer layer on the compliant GaAs substrate then the strain induced in the superlattice can be compensated sufficiently, making superlattice stable [28].

In this chapter, we employ two different approaches to achieve large valence band splitting and thin constituent layers for the InAs/GaInSb superlattice material system. The first approach is to increase the InSb composition in the GaInSb alloy. The second approach is to increase the thickness ratio between the InAs and GaInSb superlattice layers. In the first approach, we tried to keep the average lateral lattice constant (in-plane lattice constant) of the superlattice to be equal to the lattice constant of the substrate ($a_{\parallel} = a_s$) thus, the strain induced in the superlattice could be compensated sufficiently, making superlattice stable. In

the second approach, it is noted that increasing the thickness ratio could make the strain in the superlattice uncompensated, allowing small misfit within the superlattice layers.

## 6.3.1 Increasing the InSb Composition

In this approach, we increased the InSb composition while keeping the average lateral lattice constant of the superlattice to be equal to that of the substrate. The in-plane lattice constant ($a_\parallel$) is intermediate between the unstrained lattice constants of the multilayer constituents and Matthews and Blakeslee first obtained an expression of $a_\parallel$ as [96]

$$a_\parallel = a_A \left[ 1 + f_0 \left/ \left( 1 + \frac{G_A h_A}{G_B h_B} \right) \right. \right],$$
(6.3)

where $G_i$ are the shear moduli, $h_i$ the layer thickness, and the misfit between the constituent layers is given by $f_0 = (a_B - a_A)/a_A$ when $a_B < a_A$. Since the net strain of above bi-layer is zero in each period, structurally stable multi-layers may be grown on substrates having lattice constant of $a_s = a_\parallel$. With the fixed value of lattice constant of GaSb substrate, we can calculate the appropriate layer thickness ratio of superlattice $h_A/h_B$ for each InSb mole fraction of GaInSb from Eq. (6.3) as shown in Figure 6.2. Then, we can get the layer thickness of constituent layers for each detection wavelength. Figure 6.3 shows the calculated results based on the first approach. In this figure, valence band splitting is increased with the increment of InSb composition in the GaInSb alloy. However, the peak of valence band splitting is at 20% of InSb composition for 9 μm detection and at 30% of InSb composition for 11, 13, 15, and 17 μm detection, respectively. For over 30% of InSb composition the band splitting is saturated or decreased (for 9 μm detection). Though higher

InSb composition is better for large valence band splitting, this result revealed that higher InSb composition over the values shown above do not have any advantages for obtaining larger valence band splitting. Since higher InSb composition is not desirable in the superlattice layer growth, knowing the saturation point of the valence band splitting for each detection wavelength, we can choose the most desirable composition of InSb in the design of InAs/GaInSb superlattice detectors. The calculated valence band splitting value is mostly twice higher than the energy gap, and is large enough to suppress the Auger recombination rate by preventing hole-hole collisions according to the suppression mechanism [25]. From the calculated result, we know that the increasing rate of light holes ($E_{LH1}$) is much greater than that of the heavy holes ($E_{HH1}$) at low InSb composition while above the saturation point the changing rate remains the same or decreases (for 9 $\mu$m). Therefore, the valence band splitting reaches a maximum value and remains at the saturated value for over 11 $\mu$m detection wavelength while decreases for 9 $\mu$m detection wavelengths. From Figure 6.2 it is noted that each thickness ratio between the InAs and GaInSb layers for each InSb composition is linearly increased with the increment of InSb composition when we keep $a_s = a_{\parallel}$. The result shows that in this approach there are two ways to increase the valence band splitting: higher InSb composition and larger thickness ratio $h_A/h_B$. If the InSb composition is increased and $a_s = a_{\parallel}$, it is evident that the thickness ratio will also increase because for larger InSb composition a thinner GaInSb layer is required to keep $a_s = a_{\parallel}$. Total thickness change of one period of superlattice as increasing InSb mole fraction is shown in Figure 6.4. When InSb composition is increased, the total thickness of each period is decreased until around 30% of InSb composition and saturated. Since thinner layer is required for large absorption coefficients, larger InSb composition is desirable by this result until the InSb

composition reaches 35%. The result reveals that increasing above 30% of InSb composition is no longer beneficial for obtaining large absorption coefficients. The relationship between the thickness of GaInSb layer and the wavelength for the case of $a_s = a_\parallel$ is shown in Figure 6.5. In this figure, when the InSb composition is increased the slope is increased and the line is shifted to the left. This result shows that it is more difficult to control the exact wavelength for higher InSb composition because a small change in GaInSb thickness causes a large change in detection wavelength. This is one of the reasons why higher InSb composition should be avoided in the design of these type-II superlattice detectors. Through the first approach, we have designed five optimized InAs/GaInSb type-II superlattice IR detectors with $a_s = a_\parallel$. The compositions and layer thickness for these detectors are given by: 38.9 Å/16.3 Å InAs/Ga$_{0.80}$In$_{0.20}$Sb for 9.01 μm ($\Delta E_{h-1} = 0.2094$ eV); 45.7 Å/13.3 Å InAs/Ga$_{0.70}$In$_{0.30}$Sb for 11.01 μm ($\Delta E_{h-1} = 0.22678$ eV); 48.8 Å/14.2 Å InAs/Ga$_{0.70}$In$_{0.30}$Sb for 13.1 μm ($\Delta E_{h-1} = 0.24078$ eV); 50.5 Å/14.7 Å InAs/Ga$_{0.70}$In$_{0.30}$Sb for 14.83 μm ($\Delta E_{h-1} = 0.24678$ eV); 52.6 Å/15.3 Å InAs/Ga$_{0.70}$In$_{0.30}$Sb for 16.84 μm ($\Delta E_{h-1} = 0.25478$ eV). The valence band splitting for these compositions correspond to the maximum points at $\Delta E_{h-1}$ plot for each specified wavelength.

### 6.3.2  Increasing Thickness Ratio

In another approach, we increase the thickness ratio between InAs and GaInSb layers for the fixed InSb composition allowing small misfit within the superlattice layers. Figure 6.6 shows the calculation results of the valence band splitting for the 9-17 μm detection wavelengths when the thickness ratio between the InAs/GaInSb layers is increased. It should be noted that the data point on the far left of this figure for each composition represents the

result calculated from the first approach. In addition, for smaller thickness ratio than the case used in the first approach (not shown), excess tension exists in the superlattice and the micro-crack might be created in the superlattice layers. Therefore, in this study we did not consider the case of thickness ratio smaller than that of the first approach. From this figure, we know that for the 17 μm detection wavelength with high InSb composition, increasing the thickness ratio does not cause large increase in the valence band splitting. Therefore, the increment of $\Delta E_{h-1}$ is not sufficient to justify the consequence of allowing misfit in the superlattice, which could be the potential problem when the misfit becomes large at high InSb composition. Thus, only when InSb composition is around 10%, we can expect the advantage of increasing the thickness ratio in the superlattice layers. We obtained similar results for other detection wavelengths. When InSb composition is equal to 10% in the GaInSb alloy, the maximum splitting of valence band occurs at a thickness ratio of 3.0 for $\lambda_p$ = 11, 15 and 17 μm while the maximum splitting occurs at a thickness ratio of 2.5 and 2 for $\lambda_p$ = 13 and 9 μm, respectively. The change of the total thickness of one superlattice period as increasing the thickness ratio is shown in Figure 6.7. In this figure, it is noted that the total thickness of one period of superlattice has its minimum value at the thickness ratio between 2 and 2.5. At this thickness ratio, the total thickness is minimized and almost matches to the point where the superlattice has its maximum value of valence band splitting. From this result, we can choose easily the optimum thickness ratio between 2 and 3 for the InAs/GaInSb superlattice detector design. At these thickness ratios, the misfits in the superlattices are much smaller than the misfit of 48 Å InAs/ 30Å GaSb superlattice IR detector reported [28]. Therefore, the use of this second approach can be beneficial in the type-II IR detector design. From the above results, we have obtained five optimized designs

of the InAs/GaInSb type-II detectors. The composition and superlattice parameters are given by: 40.4 Å/20.2 Å InAs/Ga$_{0.90}$In$_{0.10}$Sb for 9.04 μm ($\Delta E_{h-l}$ = 0.1935 eV, thickness ratio $h_A/h_B$ = 2); 47 Å/18.8 Å InAs/Ga$_{0.90}$In$_{0.10}$Sb for 10.96 μm ($\Delta E_{h-l}$ = 0.2025 eV, $h_A/h_B$ = 2.5); 50 Å/20 Å InAs/Ga$_{0.90}$In$_{0.10}$Sb for 13.04 μm ($\Delta E_{h-l}$ = 0.2115 eV, $h_A/h_B$ = 2.5); 56.4 Å/18.8 Å InAs/Ga$_{0.90}$In$_{0.10}$Sb for 15.29 μm ($\Delta E_{h-l}$ = 0.2155 eV, $h_A/h_B$ = 3); 58.5 Å/19.5 Å InAs/Ga$_{0.90}$In$_{0.10}$Sb for 17.2 μm ($\Delta E_{h-l}$ = 0.2215 eV, $h_A/h_B$ = 3). For 15 μm and 17 μm, we choose the thickness ratio of 3.0 as the optimum point even though the minimum total thickness was obtained at a thickness ratio of 2.5. We confirmed our simulation method was valid after comparison with the reported data by Talwar *et al.* [82] as shown in Table 6.1.

## 6.4 Characterization of InAs/GaInSb Type II IR Detectors

From the simulation results depicted in the previous sections, we designed, fabricated, and characterized two InAs/GaInSb type II IR detector samples based on the two different simulation approaches as shown in Figure 6.8. We named the detector for $\lambda_c$ = 14.83 μm as "Detector A" and the sample for $\lambda_c$ = 10.96 μm as "Detector B". The samples were grown on (100) semi-insulating GaAs substrate using MBE technique. Top of the grown layers was InAs cap layer and an active layer was composed of InAs and Ga$_{1-x}$In$_x$Sb superlattices. To solve large leakage current problem, we inserted a 200Å AlSb insulating layer between the active layer and the thick GaSb buffer. These wafers were grown by SVT Associates, Inc.

### 6.4.1 Fabrication and Characterization

We used the standard photolithography process to prepare samples for dark I-V and photoresponse measurements. For the grown wafers based on InAs/Ga$_{1-x}$In$_x$Sb type-II

superlattices, the wet-chemical etching method did not work well and the wet-etched surfaces are usually so rough and difficult to make good metal contacts. Therefore, we carried dry-etching using ICP machine and had clean and exact etched profiles of a 400 × 400 $\mu m^2$ mesa structures on the wafer. After finishing the $Si_3N_4$ passivation on etched batches we made metal contacts (Ti/Au, 300Å/2000Å) for by E-beam evaporation. Since type-II SL IR detectors can absorb normal incident IR radiation, there is no need to prepare the 45° degree facet samples.

We performed the dark I-V measurements using HP4145B. As shown in Figure 6.9, the dark currents for both samples were very large even at considerably low temperature (77K) and the introduction of AlSb insulating layer to suppress the leakage currents through thick GaSb buffer layer were not effective for reducing large dark currents. From the photoresponse measurement of Detector A and B no photoresponse was observed in both samples due to the extremely high dark currents, most likely thanks to trap-assisted tunneling. One possible reason for the high dark currents could be the dislocation threading formed in the superlattice layers during the epilayer growth, which could degrade the quality of the layer structure and the devices.

### 6.4.2 Proposal of InAs/GaInSb Type II IR Photodiodes

One of the key issues in improving the InAs/GaInSb type II detector system is to develop growth technique for producing high quality type-II SL IR detector samples. As mentioned by H. Mohseni *et al.* [97], semi-insulating GaSb substrates do not exist and efforts to grow isolating GaSb or AlSb epilayers on GaSb substrates have not been very successful. In spite of these difficulties they have reported some improvements in detector

performance while optimizing the GaSb buffer growth on the GaAs substrate, which has similar device structure as our design [97,98]. Optimization in GaSb buffer growth on the GaAs substrate is worthy to try for our photoconductor design. We propose here a new design of InAs/GaInSb photodiode as shown in Figure 6.10. Some research groups have reported successful growth of IR photodiodes using InAs/GaSb or InAs/GaInSb on GaSb substrates [90,99,100]. While still using previous superlattice designs, we propose an InAs/GaInSb photodiode for long wavelength IR detection with cutoff wavelengths at $\lambda_C$ =14.83 and 10.96 μm. The layer structure consists of a 1 μm GaSb buffer/contact layer doped with Be deposited on $p$-type GaSb substrates. Then, a 0.5 μm thick InAs/GaInSb:Be $p$-layer, 1.5 μm nominally undoped InAs/GaInSb $i$-layer, and 0.5 μm InAs:Si/GaInSb $n$-layer are grown subsequently to form a $p$-$i$-$n$ photodiode.

## 6.5 Conclusions

In this Chapter, we have calculated the critical thickness of superlattice, in which the misfit dislocation is seemingly formed in the bulk superlattice and at the interface, and used it as a guide to limit the thickness of superlattice in detector design. For the purpose of the optimal design of InAs/GaInSb type-II superlattice IR detector with respect to the thickness of superlattice layer and InSb mole fraction, we employed two approaches: increasing the InSb mole fraction while keeping $a_s = a_\parallel$ and increasing the thickness ratio of constituent layers for allowing small misfit. In the first approach, we have found that the valence band splitting is increased with increasing InSb mole fraction, and then saturated or decreased depending on the detection wavelength. In the second approach, the advantages of increasing thickness ratio in obtaining large valence band splitting were obtained only for low InSb

mole fraction (less than 15% of InSb). In addition, to maximize the absorption coefficients of the superlattice, we have also investigated the effects of the two approaches on the layer thickness. In the first approach the total layer thickness of one period of superlattice was found to decrease with increment of InSb mole fraction and from around 30 % of InSb the thickness was kept at a constant value while in the second approach the minimum value of total thickness for varying the thickness ratio was found at a thickness ratio of 2 to 2.5, where we obtained the maximum valence band splitting. Using both approaches, we could successfully achieve large enough valence band splitting to effectively suppress the Auger recombination rate with sufficiently thin superlattice layers and large absorption coefficients for high performance IR detector applications in the LWIR and VLWIR spectral regimes. Based on these simulations, we have designed and fabricated two type-II superlattice IR detectors based on InAs/GaInSb material systems. Unfortunately, due to the inherent problems in GaSb-based type II photoconductor such as large leakage current and difficulty in wafer growth, we were unsuccessful in getting any observable photo-response from these detectors.
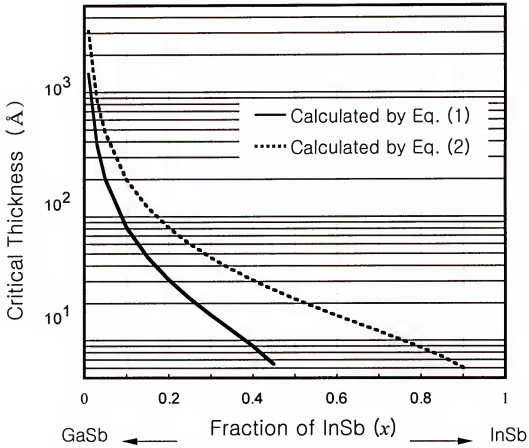
Figure 6.1. Critical thickness of Ga$_{1-x}$In$_x$Sb calculated by Eq. (1) (solid line) and Eq. (2) (dotted line).
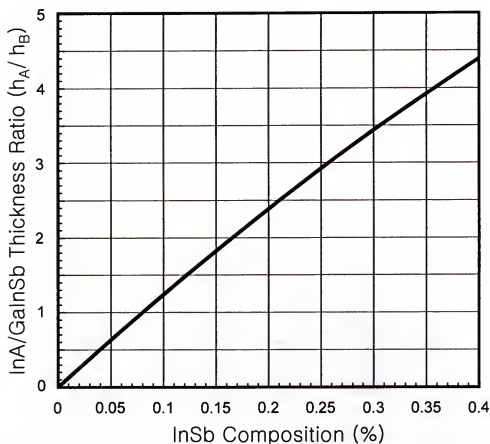
Figure 6.2. Thickness ratio of InAs/GaInSb when the average lateral lattice constant of superlattice is equal to lattice constant of the substrate $a_s = a_{\parallel}$.
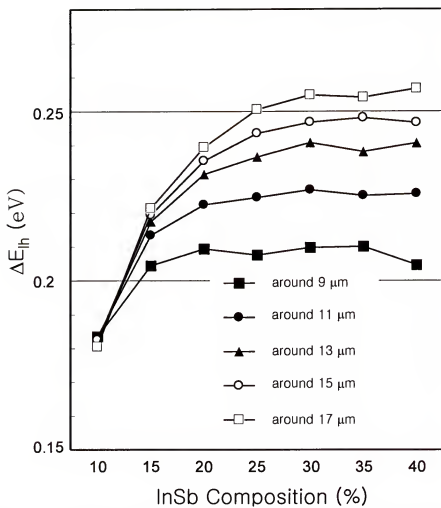
Figure 6.3. Change of valence band splitting versus InSb composition in GaInSb when $a_s = a_{\parallel}$.
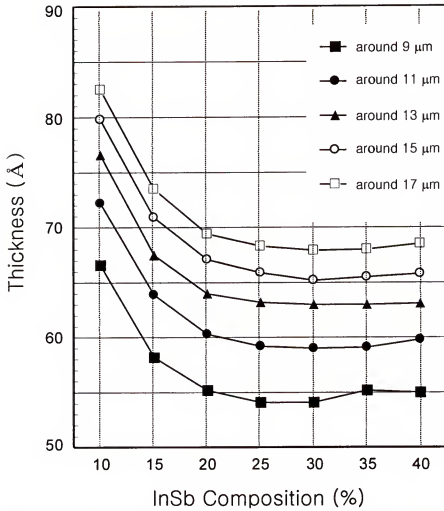
Figure 6.4. Total thickness change of one superlattice period as InSb composition increases when $a_s = a_{\parallel}$.
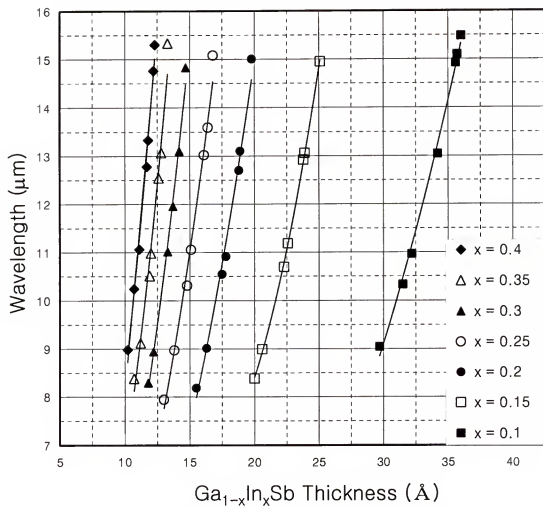
Figure 6.5. The detection wavelength versus GaInSb thickness when $a_s = a_{\parallel}$.
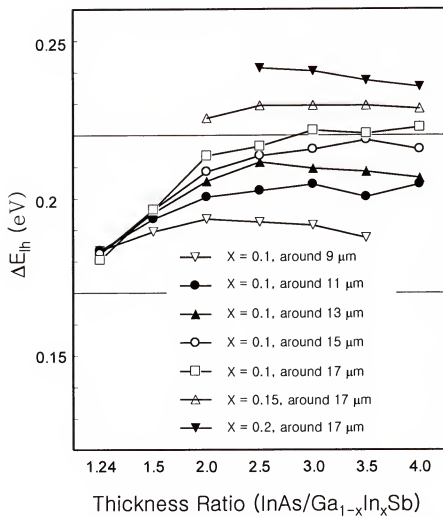
Figure 6.6. Valence band splitting versus thickness ratio while small misfit is allowed in the superlattice.
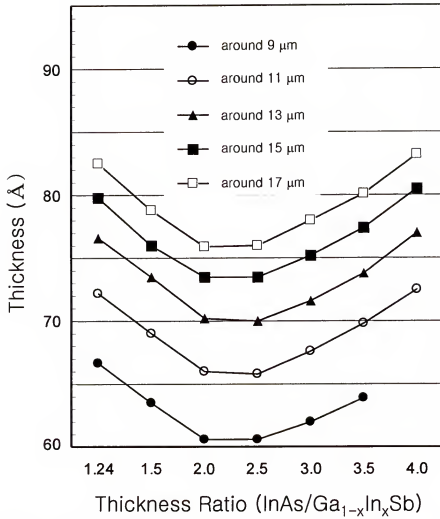
Figure 6.7. Total thickness of one superlattice period versus thickness ratio while small misfit is allowed in the superlattice.

Table 6.1. Comparison of $E_{gs}$ simulation result with reported data

| $\Delta$(C1-HH1) | Calc.(1) | Calc.(2)[*] | Expt.[*] |
|---|---|---|---|
| InAs/Ga$_{0.76}$In$_{0.24}$Sb (37Å / 25Å) | 149.9 m eV | 152±10 m eV | 136 m eV |
| InAs / Ga$_{0.74}$In$_{0.26}$Sb (41Å / 25Å) | 114.2 m eV | 111±10 m eV | 118 m eV |
| InAs / Ga$_{0.71}$In$_{0.29}$Sb (38Å / 24Å) | 125.5 m eV | 97±10 m eV | 124 m eV |

\* Calculation (2) and experimental results are from Talwar *et al* [82]



Figure 6.8. The characterized InAs/GaInSb type II superlattice detectors from simulations for characterization.
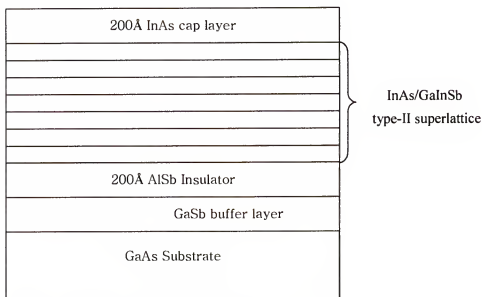
**Detector A**
150periods ($\approx$0.98 µm), For  $\lambda_c$ = 14.83 µm
50.5Å InAs/14.7Å Ga$_{0.7}$In$_{0.3}$Sb, 1 µm GaSb buffer

**Detector B**
150periods ($\approx$0.99 µm), For  $\lambda_c$ = 10.96 µm
47Å InAs/18.8Å Ga$_{0.9}$In$_{0.1}$Sb, 2 µm GaSb buffer

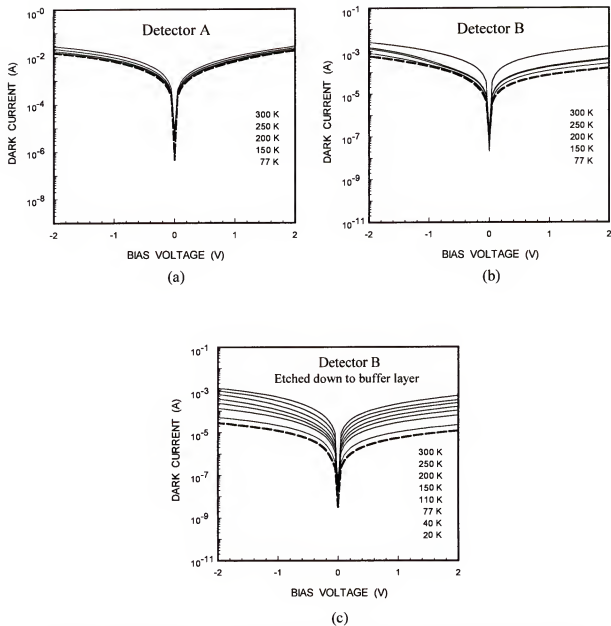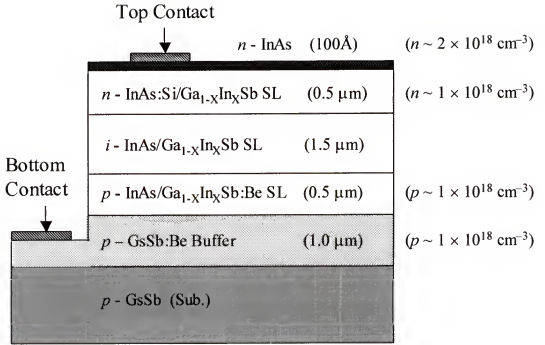Figure 6.9. The dark current versus bias voltage (I-V) curves measured for (a) Detector A, (b) Detector B and (c) over-etched Detector B at various temperatures.

Figure 6.10. The proposed InAs/GaInSb type II superlattice photodiodes from simulations for characterization.

CHAPTER 7

InGaAsSb PHOTODIODES USING TYPE II SUPERLATTICE LAYERS

## 7.1 Introduction

An InGaAsSb alloy system, grown lattice matched to GaSb, have received increased attention due to their potential applications in detectors and emitters in the $1.7 - 4.3$ μm infrared detection range. With an advantage of operating at higher temperature or at room temperature InGaAsSb infrared detectors satisfy the requirement of practical opto-electronic system applied to outdoor environmental monitoring and the military. B.L Carter *et al.* reported a high detectivity InGaAsSb *pin* IR detector grown on the GaSb substrate for blood glucose monitoring [101]. This short wavelength infrared (SWIR) detector has InAs/AlGaSb window layer to have the cut-on wavelength of 1.4 μm and is latticed matched to GaSb substrate. It showed great responsivity and detectivity at room temperature. Since the thickness of *i* layer in *pin* photodiode is critical on device performance including sensitivity and detection range it is important to know the appropriate *i* layer thickness for improving device performance.

In this chapter, we report a high detectivity InGaAsSb *pin* IR detector grown on the GaSb substrate with the modified *i* layer thickness and compare the effects of *i* layer thickness by characterizing the two photodiodes with the identical structure except different *i* layer thickness.

## 7.2 Device Design and Fabrication

InGaAsSb *pin* IR detectors grown on the GaSb substrate for 1.4 to 2.4 µm SWIR detection using type II superlattice (SL) window layers with two different *i* layer thicknesses have been fabricated and characterized. An InGaAsSb *pin* IR detector reported by B.L Carter *et al.* [101] showed very high responsivity and detectivity. To study the effects of the thickness of *i* layer of the *pin* photodiode on the performance of these devices, we doubled up the thickness of *i* layer from 1.5µm (Detector A) to 3 µm (Detector B). Figure 7.1 shows the schematic of the processed device grown by molecular beam epitaxy on a *p*-GaSb substrate. It consists of a 4000 Å *p*-GaSb buffer layer, a 5000 Å *p*-$In_{0.19}Ga_{0.81}As_{0.17}Sb_{0.83}$ ($\lambda_g$ = 2.4 µm) *p*-clad, a 1.5 (Detector A) or 3 (Detector B) µm unintentionally doped *i*-$In_{0.19}Ga_{0.81}As_{0.17}Sb_{0.83}$ ($\lambda_g$ = 2.4 µm) absorption layer, a 1.5 µm strain compensated superlattice *n*-clad ($\lambda_g$ = 1.4 µm) using 11 Å InAs and 27 Å $Al_{0.6}Ga_{0.4}Sb$ layer, and a 100 Å *n*-InAs contact layer. InAs/$Al_{0.6}Ga_{0.4}Sb$ superlattice window layer was chosen to block shorter wavelength lights and to allow the biased I-V measurement by 1.55 µm laser even though we didn't need to carry out it at this time. We can expect an improved performance from adaptation of the type-II superlattice window layer.

Photodetectors with active mesa area of 400 µm × 400 µm were fabricated by using standard photolithography and wet chemical (Detector A) or dry (Detector B) etching procedures. A $H_3PO_4$:$H_2O_2$:$H_2O$ (1:1:10) solution was used for wet chemical etching on 'Detector A' with the etching rate of around 50 Å/sec. Dry etching on 'Detector B' was performed by Plasma-Therm 790 ICP system since wet chemical etching on Detector B was not applicable due to its increased active layer. Dry etching gives GaSb based structures fine etching profile and smooth surface up to 8 µm of etching depth in our trials while generally

wet chemical etching on GaSb based structures were not successful over 3 μm of etching depth. After the passivation of $Si_3N_4$ (2000Å) for reducing leakage current, ohmic contacts of Ti/Au (300Å/2000Å) were deposited by e-beam evaporation. No annealing was done for these devices and these batch samples were bonded on the TO-8 header for electrical connection and then mounted in the Oxford closed cycle cryogenic system for low temperature measurement. The dark I-V measurement, which is followed by the spectral responsivity measurement and the calculation of detectivity were accomplished to characterize the device performance.

## 7.3 Results and Discussion

### 7.3.1 Responsivity

In this detector, the long wavelength cutoff is determined by the bandgap energy of the absorption layer while the short wavelength cut off is adjusted by the bandgap of the *n*-clad on the incident side of the junction with little effect on other aspects of photodetector performance. The bandgap energy of the absorption layer ($In_{x=0.19}Ga_{0.81}As_{y=0.17}Sb_{0.83}$) is calculated by [102]

$$E(x,y) = 0.726 - 0.961x - 0.501y + 0.08xy + 0.415x^2 + 1.2y^2 + 0.021x^2y - 0.62xy^2. \quad (7.1)$$

To calculate the short wavelength cut off of the *n*-clad type II superlattice layer using InAs/AlGaSb, we first have to consider the strain effects on each conduction and valence energy band of the superlattice layers. Using the shifted band structure, we can calculate the energy levels of each band ($C_1$ in the conduction band and $HH_1$ and $LH_1$ in the valence band) by

TMM. By combining these energy levels into one figure properly as shown in Figure 7.2 (a) we can determine the short wavelength cut off ($HH_1$ to $C_1$ transition).

The spectral responses of Detector A and B were measured by front illumination using a 1/8 m monochromater, a calibrated blackbody IR source (T = 1273 K), and a cryogenic system under various temperatures (77 K ~ 300 K). Since this photodetector shows very good performances around room temperature as well as under 250 K, we measured the spectral responsivity at 250 K and 300 K as shown in Figure 7.3. The maximum spectral responsivities of Detector A are 1.64 A/W (250 K) and 1.44 A/W (300 K) at 1.7 μm, respectively. The maximum responsivites of Detector B are 1.37 A/W (250 K) and 1.11 A/W (300 K) at 2.1 μm. After measuring the responsivity at different bias conditions as shown in Figure 7.2 (b), we characterized this detector at zero bias (photovoltaic mode) to get reliable results and utilize attractive advantages such as low dark current and low-power dissipation. In order to block unnecessary shorter wavelength lights for the purpose of noise reduction, which are outside the interested spectral range (2 ~ 2.4 μm), we used InAs/AlGaSb ($\lambda_C$ = 1.4 μm) superlattices as a window layer. The adoption of the window layer can give these detectors an improved performance since the substantial decrease in the surface recombination velocity due to the window layer could largely improve the internal quantum efficiency compared with that without window layer [103]. These responsivity graphs show excellent agreement with the initial design consideration and theoretical calculation for both detectors since shorter-wavelength lights ($\lambda < 1.4$ μm) are suppressed in this device and its cutoff wavelength is around 2.4 μm. Comparing the magnitudes of responsivity for two detectors, we did not see any significant improvement through doubling the number of periods but there is the dissimilarity in the responsivity

contours for lower detection wavelength range (1.4 – 2.0 μm). While these detectors performs like the broadband detectors and they give stable and very high responsivities for wavelengths of interest for chemical sensing (2 ~ 2.4 μm), the responsivity for Detector B increases as wavelength increasing up to 2.0 μm.

The thickness of $i$ layer in a $p$-$i$-$n$ photodiode is critical on the device performance including sensitivity and detection range, and hence we should know the appropriate $i$ layer thickness for improving device performance. One of the main reasons in increasing $i$ layer thickness of a $p$-$i$-$n$ photodiode is for most of the incident photons to be absorbed in the depletion region. Since there is no significant difference between the responsivity magnitudes of both detectors, we can say the internal quantum efficiencies for both detectors nearly close to 1 and the thickness of $i$ layer of 1.5 μm is large enough for these device systems. For the lower responsivity of Detector B compared with that of Detector A in shorter-wavelength range (1.4 – 2.0 μm) we can attribute it to wider $i$ layer of Detector B due to doubled thickness. Wider $i$ layer of Detector B made relatively more excess carriers generated by shorter-wavelength photons confined within $n$ type window layer region. While the excess carriers generated near the junction will diffuse toward the $i$ – region, for excess carriers generated by short-wavelength photons in the window layer only a fraction of them will be collected and contributed to the photocurrent and the rest of them will be easily recombined [104]. It means strongly confined photons in window layer caused lower contribution from shorter-wavelength photons to photocurrent and consequently it gave Detector B relatively selective detection contour in the interested spectral range (2 ~ 2.4 μm) for monitoring glucose level.

### 7.3.2  Dark Current and the Spectral Detectivity

The dark current-voltage (I-V) curves measured at room temperature are shown in Figure 7.3 (a) and (b). The dark current at bias voltage of - 0.5 V is - 80.9 μA for detector A and - 77.3 μA for Detector B. In reverse bias, the dark current increases constantly with bias and there is no definite breakdown. These results are similar to some reported InGaAsSb *pin* detectors [105,106]. The rising current at low positive bias causes saturation to device operation and easily makes devices inactive at higher bias (V>0.05 V) as shown in Figure 7.2 (b). The difference between dark current magnitudes of detectors is small and negligible in spite of their difference in thickness. The detectivity $D^*$ was obtained from the measured dark current and the responsivity of device $R$ using

$$D^* = R\sqrt{\frac{R_0 A}{4kT}}, \tag{7.2}$$

where $T$ is the operation temperature in degrees Kelvin and $R_0$ is the zero-bias differential resistance. Both detectors show very high detectivity of 2.2 x $10^{10}$ cm-Hz$^{1/2}$/W for Detector A at λ = 2.0 μm and 5.15 x $10^{10}$ cm-Hz$^{1/2}$/W for Detector B at λ = 2.1 μm, respectively at T = 300 K.

### 7.4 Conclusions

In conclusion, two high detectivity InGaAsSb *pin* IR photodiodes grown on the GaSb substrate with the modified *i* layer thickness are reported and the effects of *i* layer thickness on InGaAsSb *pin* photodiodes for SWIR detection have been studied. Excellent responsivity and detectivity have been obtained for both photodiodes regardless of the difference in *i* layer thickness. The maximum responsivity and peak detectivity at 300 K

were found to be 1.43 A/W and 2.2 x $10^{10}$ cm-Hz$^{1/2}$/W at 2.0 $\mu$m for Detector A and 1.11 A/W and 5.15 x $10^{10}$ cm-Hz$^{1/2}$/W for Detector B at $\lambda$ = 2.1 $\mu$m, respectively. While $i$ layer thickness of 1.5 $\mu$m must be enough for maximum sensitivity in this system the increased $i$ layer thickness give this device relatively selective detection. Increased thickness caused a difficulty in wet chemical etching process due to usually poor-grown wafer quality of GaSb-based system. By using dry etching with Plasma-Therm 790 ICP system we could get precise and clean etching profile. The wet chemical etching and dry etching on GaSb-based system will be discussed in details in Chapter 8. In addition to the efforts to optimize the structural design and growth of this system, sulphur passivation could be considered to increase the durability of the detectors with lower dark current [107].
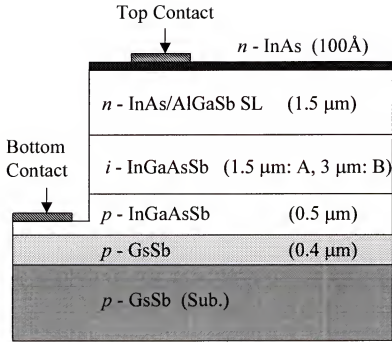
Figure 7.1. Schematic diagram of InGaAsSb photodiode with SL type II SL InAs/AlGaSb window layer on GaSb substrate for short-wavelength (2.0-2.4 μm) infrared detection.

$Al_{0.6}Ga_{0.4}Sb/$ InAs/ $Al_{0.6}Ga_{0.4}Sb$

27 Å    11 Å    27 Å

C1

C.B.

HH1

V.B.

$\Delta(C1-HH1) = 0.861$ eV

(a)



Responsivity versus bias at 250 and 300K

(b)

Figure 7.2. (a) The schematic energy band diagram of InAs/AlGaSb superlattice window layer and (b) the spectral responsivity versus bias of Detector B at 250 and 300K.

Figure 7.3. The spectral responsivity of InGaAsSb photodiodes for SWIR detection measured at 250 K and 300 K.

(a)



(b)

Figure 7.4. (a) the dark current-voltage (I-V) measurement at room temperature for detector A and (b) detector B.

CHAPTER 8
FOCAL PLANE ARRAY OF QWIP AND TYPE II IR DETECTOR FOR IMAGING
ARRAY APPLICATIONS

### 8.1 Introduction
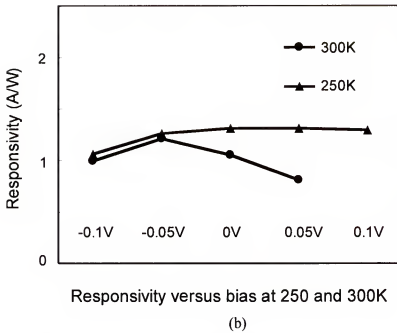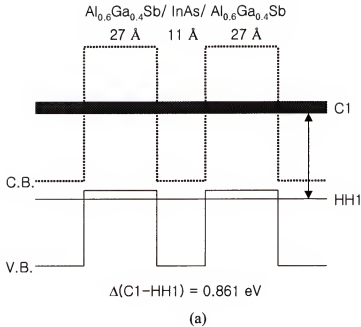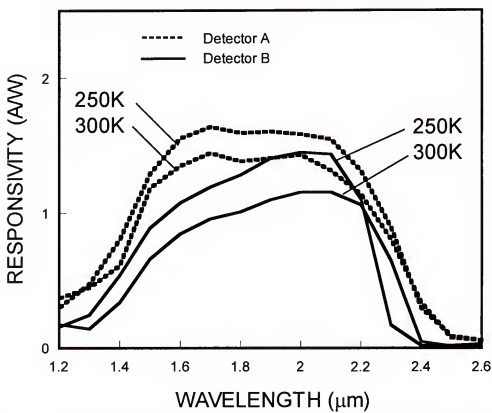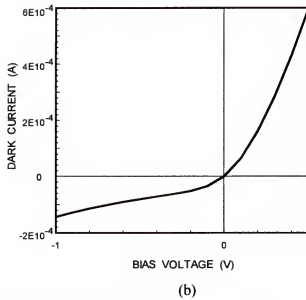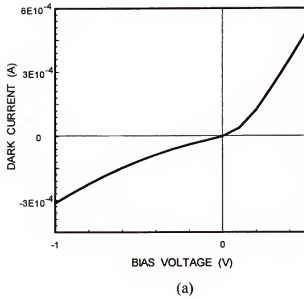
Recently, infrared (IR) focal plane arrays (FPAs) based on quantum-well infrared photodetectors (QWIPs) have found many commercial and military applications, such as mine detection, surveillance, public safety, missile detection, etc [103]. Though single-color FPA is useful for distinct targets, multi-color FPA with two or more spectral bands can improve the overall performance when the targets are not clear [104]. Due to the well-established GaAs material and processing technology multi-color QWIPs have been successfully demonstrated [35,36], and hence the advanced FPAs with multi-color QWIPs have been rapidly developed. Sanders reported a two-color 256 x 256 bound-to-miniband QWIP FPAs for the first time and a two-color large 640 x 486 GaAs/AlGaAs FPA for LWIR and VLWIR bands was developed by P. L. McCarley *et al.* [106]. Currently, while 1024 x 1024 extra large FPA is commercially available using QWIP Technologies, and the large format high uniformity and low cost GaAs QWIP FPAs have been successfully developed for IR imaging applications [107-109].

On the other hand, FPAs of GaSb-based type II superlattice IR detectors have attracted considerable attentions due to their promising performance for longer wavelength detection at high temperatures. However, since the study in these detectors including the growth technology and the fabrication of large scale FPAs is immature, a few research groups have reported type II FPAs thus far, and no commercialized products have been

reported as yet [110].

In this chapter, we have demonstrated a two-color, two-stack QWIP 4 x 4 FPA with dielectric grating grown on the semi-insulating (SI) GaAs substrate and proposed dielectric grating for this FPA while discussing the feasibility of large format FPAs using GaSb-based type II superlattice detectors through etching and fabrication test for GaSb wafers.

## 8.2 Two-Color Two-Stack Focal Plane Array with Dielectric Grating

### 8.2.1 Device Design and Fabrication

The dual band (LW/MW) two-stack QWIP 4 x 4 FPA were grown on semi-insulating GaAs substrate. Table 8.1 shows the complete layer structure for this LW/MW two-stack, two-color QWIP 4 x 4 FPA. Both unit cells of the top-stack for LWIR detection ($\lambda_p \cong 8.8$ μm) and the bottom-stack for MWIR detection ($\lambda_p \cong 4.2$ μm) were repeated 5 times and each stack were surrounded by the undoped 1000 Å GaAs spacer layers. The top and bottom stacks were separated by the GaAs ohmic contact layer (4500Å, Si-doped to $2 \times 10^{18}$ cm$^{-3}$) and another two GaAs ohmic contact layers were grown on the top of top-stack and the bottom of bottom-stack. Figure 8.1 shows the schematic conduction band diagrams of this FPA for (a) top-stack (LWIR), (b) bottom-stack (MWIR). As shown in Fig. 8.1, the intersubband transition schemes of LWIR QWIP stack for the 4 x 4 FPA is the bound-to-quasi-bound (BTQB) while MWIR QWIP stack employs the bound-to-continuum (BTC) transition schemes.

The dual band, two-stack 4 x 4 QWIP focal plane array (FPA) with a pixel size (100 x 100 μm$^2$) was fabricated by using wet etching and photolithography procedure. The seven masks set for 3-stack FPAs designed by Jung Hee Lee, was used to process FPA [111]. Figure 8.2 (a) shows the three-dimensional (3-D) view of a detector pixel for three-stack

QWIP 4 x 4 FPA. Figure 8.2 (b) shows the final top-view of three-color, three-stack QWIP 4 x 4 FPA: after ohmic contact metallization by e-beam evaporation and Figure 8.2 (c) is the SEM picture of the processed FPA. The mesa structures for both of the top- and bottom-stack detectors were patterned by wet chemical etching procedures. After passivation of $Si_3N_4$, the ohmic contact pattern (AuGe/Ag/Au) was deposited by e-beam machine and then annealed at T = 450$^o$C for 2 minutes. For performance comparison between QWIP 4 x 4 FPA and single QWIP detector, the test mesa structure with an active area of 216 x 216 $\mu m^2$ was also fabricated by using standard photolithography and wet chemical etching procedure.

### 8.2.2 Measurement of Dark IV and Photoresponse

For coupling the incident IR radiation into the quantum wells, the 4 x 4 array detector and the single detector were polished to 45$^o$ facet on the backside of the substrate. The spectral response was measured at T = 77 K for the LWIR BTQB-QWP (top-stack) and the MWIR BC-QWIP (bottom-stack) by using an 1/8 monochromater, a calibrated blackbody IR source (T = 1273 K), and Oxford CCC1204 closed cycle liquid helium cryostat at 200 Hz chopped frequency.

Figure 8.3 (a) and (b) show the dark current versus bias voltage (I-V) curves measured at T = 77 and 90K for the LWIR-QWIP and at T = 77 and 150K for the MWIR-QWIP of both the 2-color 2-stack single QWIP and 4 x 4 QWIP FPA. Although the dark currents for the single QWIP and the 4 x 4 QWIP array are almost identical, the dark currents of the single QWIP are one order of magnitude higher than those of the 4 x 4 QWIP array for both stacks. The reason for the higher dark current in the single QWIP is attributed to the lower sheet resistance since the active detector area of the single QWIP (46656 $\mu m^2$) is larger than that (5781.25 and 7187.5 $\mu m^2$) of one pixel of the 4 x 4 QWIP array.

Figure 8.3 shows the spectral responsivity measured at T = 77K and $V_b = \pm 2V$ for (a) top-stack and (b) bottom-stack, respectively. The responsivities for the single QWIP and the 4 x 4 QWIP are good, and the contours of curves are almost identical while the peak wavelengths for LWIR was at $\lambda_p = 8.7\ \mu m$ (under positive bias) and the peak for MWIR was at $\lambda_p = 4.2\ \mu m$. The peak responsivities for the top-stack LWIR QWIP (at $\lambda_p = 8.7\ \mu m$) were $R_i = 1.44$ and 0.33 A/W at $V_b = +2V$ and at T = 77K for the single QWIP and the 4 x 4 QWIP array, respectively. The peak responsivities for the bottom-stack MWIR QWIP (at $\lambda_p = 4.2\ \mu m$) were $R_i = 0.057$ A/W for the single QWIP and $R_i = 0.038$ A/W for the 4 x 4 QWIP array at $V_b = +2V$ and at T = 77K. The larger responsivity for the single QWIP was expected since the single QWIP has more incident lights and better light coupling due to larger detector area.

### 8.2.3 Dielectric Grating

Since the absorption of normal incident light on n-type QWIPs is prohibited by quantum mechanical selection rule for intersubband transition, we employed the 45° facet on substrate for the single detector and the 4 x 4 QWIP array as a light coupling method. However, the 45° facet could not be used for the implementation of large FPAs. For light coupling scheme for large FPA, the diffraction grating is more efficient method for large optical coupling in which the grating can scatter the incoming light perpendicular to the surface into an oblique direction for the optimized QW absorption. There are two ways to form the metal grating structure: one is to evaporate a metal (i.e, Au) directly onto the top of the detector, and the other is to etch the contact layer and cover it with thin layer of Au. The cross-grating coupler (2-demensional) can improve greatly the device performance up to 4 to

5 times higher than the 45° edge coupling [112,113]. In addition, the random scattering reflector with waveguide structure by C. J. Chen *et al.*, and the corrugated (C-) QWIP by K. K. Choi have been demonstrated, which showed a better optical coupling and an enhancement of QWIP performance [114,115].

We designed the grating structure for three-color, three-stack QWIP to couple simultaneously the three different wavelength regions (LW/MW/SW for the top-/middle-/bottom-stack) as shown in Figure 8.5 and 8.6, respectively. This grating structure is for the 4 x 4 FPA with the unit cell area of 100 x 100 $\mu m^2$. The grating structures combined by three different geometrical structures were etched onto the contact layer over the top-stack QWIP. As shown in Figure 8.5, the same areas are allocated for each grating structure and then the unit cells for each grating structure are randomly located throughout the entire area of the grating coupler. It is well known that the distance from the grating coupler to the QWIP layers and the number of the grating pixels are very important for the grating coupler efficiency. Although the grating coupler areas for each wavelength region are the same, the number of the pixels is varied because the periods of each grating structure are different. It means that the 1, 9 and 16 square grating pixels of each grating structures for LWIR, MWIR and SWIR detections can be etched in a unit cell (4.4 x 4.4 $\mu m^2$). The difference in the number of the pixels can help to reduce the concern of the less grating efficiency of MWIR and SWIR QWIPs due to relatively larger distance from the grating coupler. For the maximum electric field at a certain point in the QWIP, the usual grating equation can be expressed as [116]

$$\sin\theta = \frac{\lambda_p^{'}}{g}, \tag{8.1}$$

where $\theta$ is the diffraction angle, $\lambda_p^{'}$ is the peak wavelength in the QWIP, and $g$ is the period of the grating structure. To achieve the maximum grating efficiency, each grating structure must have its own grating pixel depth ($h$), which requires the complicated process. However, to simplify the processing steps only the one grating pixel depth was used in our fabrication, which could yield a lower grating coupling efficiency but it should not be a critical factor for the overall QWIP device performance. Finally, the dielectric grating will not be covered with the metal (Au) since E. Costard *et al.* [117] have demonstrated the MWIR QWIP with excellent performance in which the dielectric grating without metal covering was used.

### 8.2.4 Two-Color, Two-Stack QWIP 4 x 4 FPA with Dielectric Grating

For etching process of dielectric grating structure on the dual band 2-stack 4 x 4 FPA the thinner photoresist of AZ 1505 were used instead of the usual photoresist of AZ 1529 since the small grating structures needed much finer resolution. The thickness of coated AZ 1505 is 0.4 μm while that of AZ 1529 is 2.7 μm at 3000 RPM of spin speed. Since we could choose only one etching thickness of the dielectric grating for both stacks and the thickness of top contact is only 4500 Å, we etched 2000 Å down on top-stack for the margin using above grating mask.

The dark current versus bias voltage (l-V) curves were measured at various temperatures, and the spectral responsivity at T = 77K were measured through front illumination. Figure 8.7 shows the dark l-V curves measured for (a) the LWIR-QWIP and (b) the MWIR-QWIP at various temperatures. Comparing those curves from the 4 x 4 QWIP arrays with and without grating, we could notice that the dark -V curves are almost identical,

which is expected because both arrays have the identical structures and dimensions except the dielectric grating.

Figure 8.8 shows the spectral responsivity of the 4 x 4 QWIP array with grating measured at T = 77K for (a) the top-stack at $V_b = \pm 1.8$V and (b) the bottom-stack at $V_b = \pm 2$V while comparing these results with that of the 4 x 4 array without grating. The peak responsivities for the top-stack LWIR QWIP of the 4 x 4 array with grating were found to be $R_i = 0.028$ (at $\lambda_p = 8.6$ μm) and 0.04 (at $\lambda_p = 8.7$ μm) A/W at $V_b = \pm 1.8$V and at T = 77K. For the bottom-stack MWIR QWIP of the 4 x 4 array with grating, the peak responsivities at T = 77K were found to be $R_i = 0.059$ and 0.05 A/W at $V_b = \pm 2$V and $\lambda_p = 4.2$ μm. For the LWIR top-stack, the responsivities of the 4 x 4 array without grating were much higher than that of the 4 x 4 array with grating while the results were reversed for the MWIR bottom-stack. These results confirmed the fact that dielectric grating would improve the responsivity of the MWIR QWIP and also provided an idea that 2000 Å of etched grating depth was much effective on the MWIR QWIP than the LWIR QWIP. Since thicker grating is better for longer wavelength detection, we need to etch down the dielectric grating deeper for the improved performance of LWIR QWIP. Although introduction of dielectric grating for the multi-stack FPAs are not satisfied for every detection scheme, the overall performance with grating was meaningful and with optimizing of the grating depth we could get more uniformed results for broader detection range. In addition, dielectric grating can give cheaper and easier way to fabricate the FPAs than that of the metal grating.

### 8.3 FPAs of GaSb-Based Type II Superlattice IR Detectors

Type-II superlattice IR detectors based on GaSb are good candidates for infrared detection in the long and very long wavelength ranges and even more attractive due to the possibility of higher temperature operation. In spite of these assets the progress of fabricating large format FPAs using type-II superlattice detectors has been slowed by the poor wafer quality such as non-uniformity and low-reproducibility.

In this section, we studied the feasibility of large format FPAs using type-II detectors through wet chemical etching and dry etching processes on GaSb based wafers.

### 8.3.1 Wet Chemical Etching and Dry Etching on GaSb-based Wafers

The solutions such as NaK(tartrate)/HCl/H$_2$, H$_3$PO$_4$/H$_2$O$_2$/H$_2$O, Citric Acid/H$_2$O$_2$ and C$_4$H$_6$O$_6$(tartaric)/H$_2$O$_2$/HF are suggested as possible etching solutions for the GaSb-based systems. We performed wet chemical etching test to find right solution for InGaAsSb *pin* IR detectors grown on the GaSb substrate with InAs/AlGaSb window layer, which was depicted in Chapter 7. Both the C$_4$H$_6$O$_6$(tartaric)/H$_2$O$_2$/HF, which is a good etching solution of GaSb, and the conventional etching solution H$_3$PO$_4$/H$_2$O$_2$/H$_2$O were tested as shown in Table 8.2. Although we have found a new recipe (by alternating C$_4$H$_6$O$_6$(tartaric)/H$_2$O$_2$/HF and H$_3$PO$_4$/H$_2$O$_2$/H$_2$O) for the wet etching of this detector from the repeated trials, for the purpose of simplicity of fabrication process we choose the conventional H$_3$PO$_4$/H$_2$O$_2$/H$_2$O solution. For smoother etching profile, a little bit diluted solution (H$_3$PO$_4$/H$_2$O$_2$/H$_2$O, 1 : 1 : 10) was used for 'Detector A' with the etching rate of about 50 Å/sec. However, for 'Detector B' with thicker active layer, wet chemical etching was found not working. Dry etching on 'Detector B' was performed by Plasma-Therm 790 ICP system at an etching rate

of 120 Å/sec. We found that wet chemical etching on GaSb based structures were not successful over 3 μm of etching depth, but dry etching gives GaSb based structures fine etching profile and smooth surface up to 8 μm of etching depth in our trials. Etch conditions for dry etching were given as follows:

  • Power : Rf 150W / ICP 300W    • Gas : 10Cl$_2$/5Ar

  • Pressure : 5m torr       • DC bias : -261 V

Table 8.3 lists the advantages and disadvantages between the wet chemical and dry etchings.


### 8.3.2  Fabrication Test of 320 x 256 FPAs of GaSb-based Wafers

For testing the fabrication of large format type II superlattice IR detector FPAs, a 320 x 256 FPA was fabricated on the GaSb substrate. In this array structure, each pixel has area of 28 μm x 28 μm with 4μm spacing and metal contact of 20 μm x 20 μm was deposited on every pixel through Si$_3$N$_4$ passivation window. For patterning, dry etching was carried out by Plasma-Therm 790 ICP system with a 4 μm of etch depth. Since we used thinner photoresist for fine resolution, it could not endure long period of dry etching process. Therefore, we adapted 2 -layer photolithography using 2000 Å of SiO$_2$ as a mask for dry etching process as shown in Figure 8.9. Using this method, we obtained up to 8 μm of etch depth on the GaSb substrate with smooth surface and fine etching profile. Other steps used in the fabrication of this FPA followed the fabrication process of GaSb based detectors depicted in Chapter 6 and 7. Finally, a 320 x 256 FPAs was successfully fabricated on GaSb substrate as shown in Figure 8.10.

**8.4 Conclusions**

In conclusion, we have demonstrated a two-color, two-stack QWIP 4 x 4 FPA with dielectric grating. The LW/MW FPA can detect two peaks in simultaneously in LWIR region and MWIR wavebands. The introduction of dielectric grating as light coupling has improved the performance of the 4 x 4 QWIP FPA with normal incident illumination. With the successful demonstration of a 4 x 4 QWIP FPA using dielectric grating, we expect an improved performance and easier implementation of the larger format FPAs. In addition, we have fabricated a 320 x 256 FPA test structure on the GaSb substrate to study the feasibility of a larger format FPAs of GaSb based type II superlattice IR detectors.

Table 8.1. The layer structure of the LW/MW QWIP 4 x 4 FPA

| Layer | | Thickness (Å) | Dopant | Concentration (cm$^{-3}$) |
|---|---|---|---|---|
| n GaAs (top contact) | | 4500 | Si | $2\times10^{18}$ |
| i GaAs (spacer layer) | | 1000 | none | none |
| i AlGaAs | | 300 | none | none |
| i GaAs | X 5 | 5 | none | none |
| n InGaAs | | 62 | Si | $7\times10^{17}$ |
| i GaAs | | 5 | none | none |
| i AlGaAs | | 300 | none | none |
| i GaAs (spacer layer) | | 500 | none | none |
| n GaAs (middle contact) | | 4500 | Si | $2\times10^{18}$ |
| i GaAs (spacer layer) | | 1000 | none | none |
| i AlGaAs | | 300 | none | none |
| i GaAs | X 5 | 5 | none | none |
| n InGaAs | | 25 | Si | $2\times10^{18}$ |
| i GaAs | | 5 | none | none |
| i Al$_x$Ga$_{1-x}$As | | 300 | none | none |
| i GaAs (spacer layer) | | 1000 | none | none |
| n GaAs (bottom contact) | | 4500 | Si | $2\times10^{18}$ |
| S.I. GaAs substrate | | $625 \pm 25$ μm | none | none |
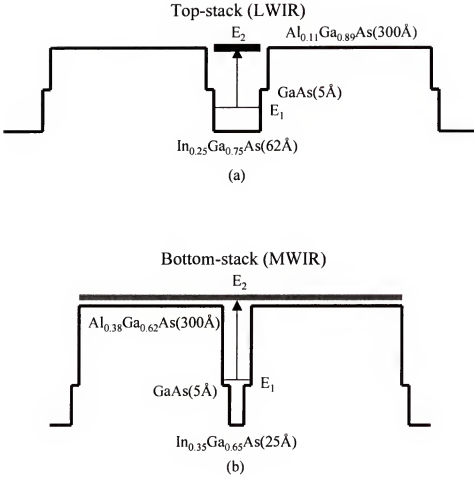
Figure 8.1. The schematic conduction band diagrams of the two-color, two-stack QWIP FPA for (a) top-stack (LWIR), (b) bottom-stack (MWIR)
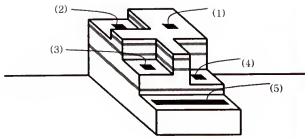
(a)
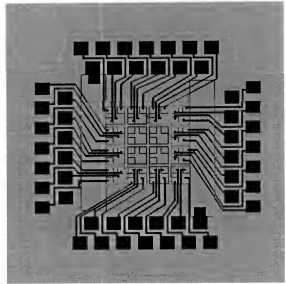
(b)
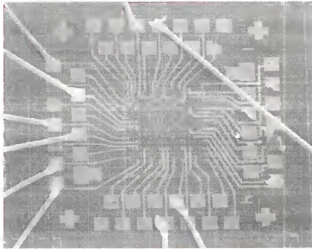
(c)

Figure 8.2. (a) The three-dimensional (3-D) view of a detector pixel for three-stack QWIP 4 x 4 FPA, (b) the final top-view of three-color, three-stack QWIP 4 x 4 FPA and (c) the SEM picture of the processed FPA.
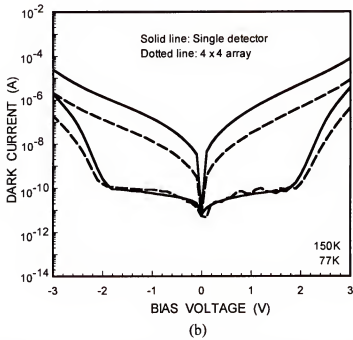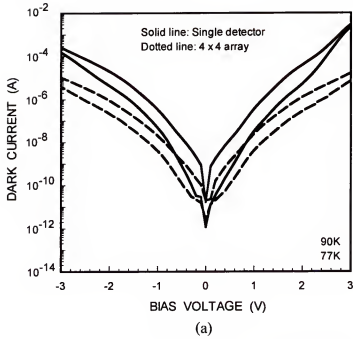
Figure 8.3. The dark current versus bias voltage (I-V) curves measured for (a) the LWIR-QWIP at T = 77 and 90K and (b) the MWIR-QWIP at T = 77 and 150K for both the 2-color 2-stack single QWIP and 4 x 4 QWIP FPA.

(a)



(b)
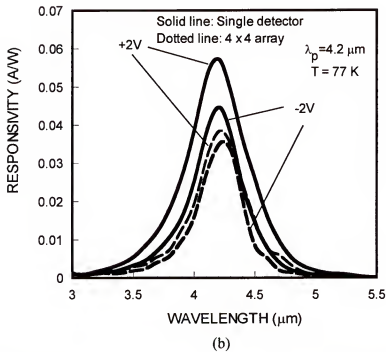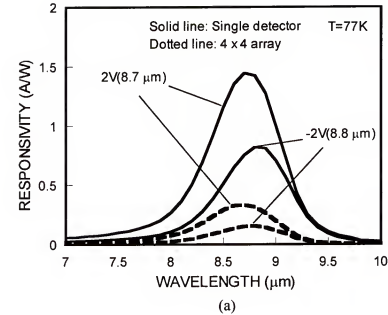
Figure 8.4. The spectral responsivity measured at T = 77K and $V_b = \pm 2V$ for (a) top-stack (LWIR) and (b) bottom-stack (MWIR).

Figure 8.5. The grating structure for three-color, three-stack QWIP 4 x 4 FPA (LW/MW/SW for top-/middle-/bottom-stack) with the unit cell area of 100 x 100 $\mu m^2$.

( Dimensions of Unit Cell 1, 2, and 3 )



Unit Cell 1: [ 1 ]   ⟹
(LWIR)

Unit Cell 2: [ 2 ]   ⟹
(MWIR)
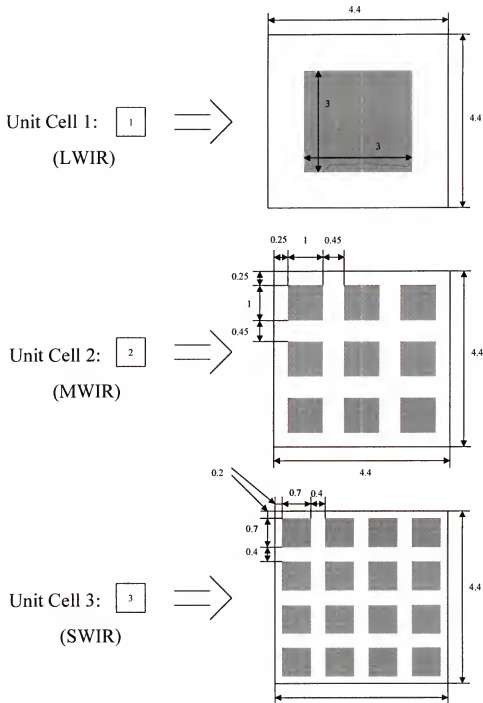
Unit Cell 3: [ 3 ]   ⟹
(SWIR)

Figure 8.6. Dimensions of the unit cell for the grating structure of the three-color, three-stack QWIP 4 x 4 FPA.

(a)



(b)
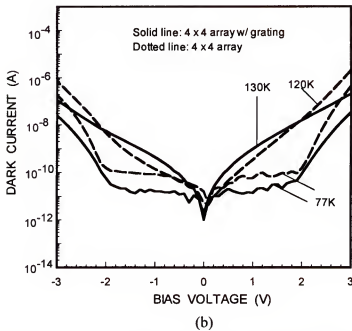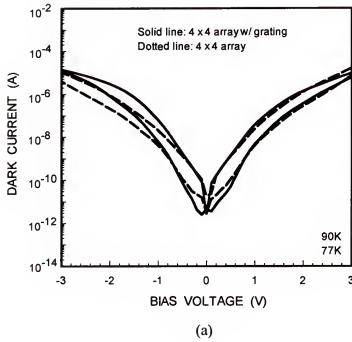
Figure 8.7. The dark I-V curves measured for (a) the LWIR-QWIP and (b) the MWIR-QWIP at various temperatures for both the 4 x 4 FPA and the 4 x 4 FPA with grating.

Figure 8.8. The spectral responsivity of the 4 x 4 arrays with grating and without grating measured under T = 77K for (a) top-stack at $V_b = \pm 1.8V$ and (b) bottom-stack at $V_b = \pm 2V$.

Table 8.2. The results of wet chemical etching on GaSb based wafers

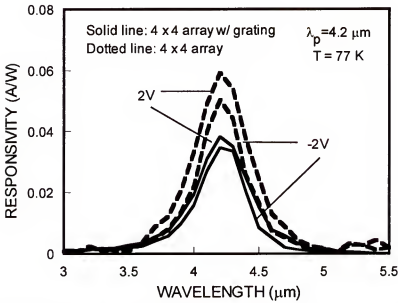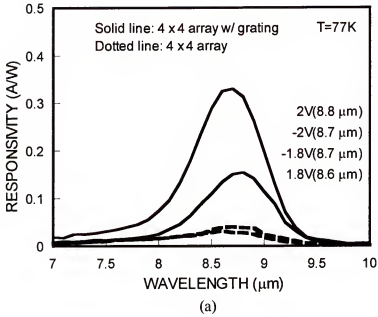| | Solution | Sample | Result | Discussion |
|---|---|---|---|---|
| 1st trial | Tartaric powder : HF : H$_2$O$_2$ : H$_2$O<br>4 : 1 : 1 : 220 | GaSb substrate | ~120Å /sec | From the results, etching on real device should be good also. |
| 2nd trial | Tartaric powder : HF : H$_2$O$_2$ : H$_2$O<br>4 : 1 : 1 : 220 | InAs/ AlGaSb | No etching | Two possible reasons ;<br>1. Tartaric acid is a little bit old (since first making)<br>- We have to use 10% solution not powder on next trial.<br>2. Tartaric acid can't etch InAs layer(top)<br>- Need re-trial on GaSb substrate. |
| 3rd trial | H$_3$PO$_4$ : H$_2$O$_2$ : H$_2$O<br>1 : 1 : 8 | GaSb substrate | ~50Å /sec | Our conventional etchant can etch GaSb. |
| 4th trial | Tartaric powder : HF : H$_2$O$_2$ : H$_2$O<br>4 : 1 : 1 : 220 | GaSb substrate | ~120Å /sec | First trial was right. This etchant can etch GaSb substrate. |
| 5th trial | Tartaric powder : HF : H$_2$O$_2$ : H$_2$O<br>4 : 1 : 1 : 220 | InAs/ AlGaSb | No etching | Tartaric acid can't etch InAs top layer.<br>Alternative recipe:<br>After etching InAs top layer using conventional etchant, etch active layer using tartaric acid. |
| 6th trial | H$_3$PO$_4$ : H$_2$O$_2$ : H$_2$O<br>1 : 1 : 8 | InAs/ AlGaSb | ~50Å /sec | Tried on top InAs layer using conventional etchant for above approach. |

Table 8.3. Comparison between Wet etching and Dry etching

| | Wet chemical etching | Dry etching |
|---|---|---|
| Pros | can control etch depth and easy to process | better uniformity, repeatability, anisotropic profiles, improved etch depth control and high aspect ratios |
| Cons | rough etched surface, isotropic etching processing | expensive, complex due to the use of ICP machine with toxic gases<br>large variation in etch rate depending on constituent materials |
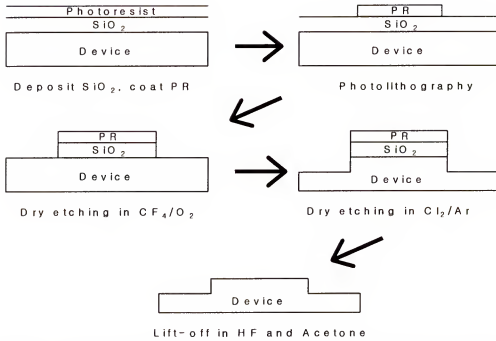
Figure 8.9. 2-layer photolithography using 2000 Å of $SiO_2$ as a mask for dry etching process.
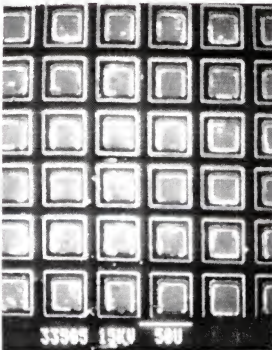


Figure 8.10. 320 x 256 Array fabricated on GaSb substrate

CHAPTER 9
SUMMARY AND CONCLUSIONS

First, we have demonstrated two novel high performance n-type quantum well infrared photodetectors (QWIPs) in this report. These QWIP structures with excellent morphology were grown by molecular beam epitaxy (MBE) technique. Multi-color and voltage-tunable detection with high performance have been achieved through single QWIP devices by using the asymmetric structure and the strain effect.

The first QWIP device was a high performance, high-strain, two-stack three-color QWIP for mid-wavelength infrared (MWIR) and long-wavelength infrared (LWIR) dual band detection. This two-stack device consists of the top stack InGaAs/AlGaAs/InGaAs TC-QWIP for LWIR and the bottom stack InGaAs/AlGaAs BC-QWIP for MWIR dual band detection. A maximum responsivity of 2.63 A/W was obtained at $\lambda_p$ = 10.3 m, $V_b$ = -7.8V, and T = 40K for the LWIR TC-QWIP. The strong quantum confined Stark shift and the rapid increase of the peak responsivity with applied bias for the $E_1$-$E_3$ transition were observed in both the LWIR TC- and stacked- QWIPs, while the peak responsivity at $\lambda_p$ = 5.1 μm due to bound-to-continuum (B-C) transition was obtained up to T = 120 K for the MWIR BC-QWIP. Though the LWIR TC-QWIP reported here used 20 periods of quantum wells, for the low background and low bias applications, short period (3-5 period) TC-QWIP structure should be used so that high peak responsivity and detectivity can be achieved in a TC-QWIP under low bias conditions.

The second QWIP was a new high sensitivity superlattice-coupled (SC)-InGaAs/GaAs/AlGaAs QWIP, which uses a SC - quantum wells and exhibits a peak detection wavelength at 10.5 $\mu$m. Excellent responsivity and detectivity due to the use of SC - quantum wells have been obtained in this device. The maximum responsivity and peak detectivity ($D^*$) at $\lambda_p$ = 10.5 $\mu$m and T = 20K under positive bias were found to be $R_i$ = 4.95 A/W and $D^*$ = 1.83 x $10^{10}$ cm-Hz$^{1/2}$/W at $V_b$ = 3.15V, respectively. Further refinement through design modification including the material composition, layer thickness, and the number of superlattice- coupled quantum wells can be made to this structure to tailor the peak wavelength and to improve the responsivity.

For the purpose of overcoming some of the disadvantages of commercially available IR detectors such as HgCdTe and QWIPs for 3-14 $\mu$m or longer wavelength detection range, type II strained layer superlattice detectors based on GaSb have been extensively studied for past over 15 years. With a variety of advantages like lower dark current, higher operating temperature and a high degree of freedom in bandgap engineering over their counterparts, type II IR detectors are becoming a promising candidate for longer wavelength range. In this work we have performed the simulation using two different approaches to obtain optimal design of type II InAs/GaInSb detectors, and characterized an InGaAsSb p-i-n photodiode using InAs/AlGaSb type II superlattice window layers.

In the simulations of type II InAs/GaInSb detectors, we employed two approaches: increasing the InSb mole fraction while keeping $a_s = a_\parallel$ and increasing the thickness ratio of constituent layers for allowing small misfit. Prior to simulations, we calculated the critical thickness of superlattice, in which the misfit dislocation is seemingly formed in the bulk superlattice and at the interface, and used it as a guide to limit the thickness of superlattice

layer in detector design. In the first approach, we have found that the valence band splitting is increased with increasing InSb mole fraction, and then saturated or decreased depending on the detection wavelength. In the second approach, the advantages of increasing thickness ratio in obtaining large valence band splitting were obtained only for low InSb mole fraction (less than 15% of InSb). In addition, to maximize the absorption coefficients of the superlattice, we have also investigated the effects of the two approaches on the layer thickness. In the first approach the total layer thickness of one period of superlattice was found to decrease with increment of InSb mole fraction and from around 30 % of InSb the thickness was kept at a constant value while in the second approach the minimum value of total thickness for varying the thickness ratio was found at a thickness ratio of 2-2.5, where we obtained the maximum valence band splitting. Through the simulation using both approaches, we successfully obtained optimal type II detector designs with large valence band splitting, thin superlattice layers and large absorption coefficients. But, the characterization of the photoconductive type-II IR detectors was not successful due to their high leakage currents. Since photodiode devices are less susceptible to large leakage current and short- out of superlattices caused by the GaSb substrate and GaSb buffer, to avoid these problems we proposed type II IR photodiodes based on our optimal designs.

We demonstrated two high detectivity InGaAsSb *p-i-n* photodiodes using type II InAs/AlGaSb superlattice window layers. InAs/AlGaSb superlattice window layer worked well for short-wavelength blocking and its detection wavelength was well matched with theoretical expectation. The effects of *i* layer thickness on InGaAsSb *pin* photodiodes for SWIR detection are studied. Excellent responsivity and detectivity have been obtained for both photodiodes regardless of the difference in *i* layer thickness. The maximum

responsivity and peak detectivity at 300 K were found to be 1.43 A/W and 2.2 x $10^{10}$ cm-Hz$^{1/2}$/W at 2.0 μm for Detector A and 1.11 A/W and 5.15 x $10^{10}$ cm-Hz$^{1/2}$/W for Detector B at $\lambda$ = 2.1 μm, respectively. While $i$ layer thickness of 1.5 μm must be enough for maximum sensitivity in this system the increased $i$ layer thickness give this device relatively selective detection. In addition to the efforts to optimize the structural design and growth of this system, sulphur passivation can be considered seriously to have durable detectors with lower dark current.

Finally, we have demonstrated a two-color, two-stack QWIP 4 x 4 FPA with dielectric grating. By comparing the performance between the single QWIP and the 4 x 4 QWIP array without grating, we confirmed the LW/MW FPA could detect two peaks in simultaneously in LWIR region and MWIR wavebands without any significant degrading. Besides, the introduction of dielectric grating as light coupling has improved the performance of the 4 x 4 QWIP FPA with normal incident illumination. With the successful demonstration of a 4 x 4 QWIP FPA using dielectric grating, we expect an improved performance and easier implementation of the larger format FPAs. In addition, we have successfully fabricated a 320 x 256 FPA test structure on the GaSb substrate to study the feasibility of a larger format FPAs of GaSb based type II superlattice IR detectors.

For the further optimization of the QWIP performance, the extended study is needed in modeling of device, improving low background characteristics, increasing operating temperature, and so on. Since infrared imaging is the main purpose for studying QWIP, more efforts are required in improving light coupling methods such as grating coupler and random scattering structures to achieve high performance and low cost FPAs.

While the growth technology is the main concern in the study of type II superlattice IR detectors, we also should focus on optimal device design including theoretical consideration on proper absorbing layer thickness and structural design to reduce leakage currents like the compliant GaAs substrate. Understanding on nano-scale structures is important to the goal of achieving higher temperature operation and wavelength tunability and technological consideration on FPA fabrication such as electron beam lithography and plasma etching techniques, should be implemented.

## REFERENCES

1. W. Herschel, Philos. Trans. R. Soc. London **90**, 284 (1800); ibid. **90**, 487 (1800).

2. C. T. Elliott and N. T. Gordon, "Infrared detectors and emitters: materials and devices," eds. P. Capper and C. T. Elliott., Kluwer Academic Publishers, 1 (2001).

3. A. Rogalski, Infrared Phys. Technol. **40**, 279 (1999).

4. B. F. Levine, J. Appl. Phys. **74**, R1 (1993).

5. Sheng S. Li, Recent Res. Devel. Quantum electronics **1**, 101 (1999).

6. L C. West and S. J. Eglash, Appl. Phys. Lett. **46**, 1156 (1985)

7. B. F. Levine, K. K. Choi, C. G. Bethea, J. Walker, and R. J. Malik, Appl. Phys. Lett. **50**, 1092 (1987).

8. D. D. Coon and R. P. Karunasiri, Appl. Phys. Lett. **33**, 495 (1984).

9. L. S. Yu and S. S. Li, Appl. Phys. Lett. **59**, 1332 (1991).

10. B. F. Levine, C. G. Bethea, G. Hasnain, V. O. Shen, E. Pelve, R. R. Abbot, and S. J. Hsieh, Appl. Phys. Lett. **56**, 851 (1990).

11. J. Chu and S. S. Li, IEEE J. Quantum Electronics **33**, 1104 (1997).

12. H. C. Liu, F. Szmulowicz, Z. R. Wasilewski, M. Buchanan, and G. J. Brown, J. Appl. Phys. 85, 2972 (1999).

13. M. A. Kinch and A. Yariv, Appl. Phys. Lett. **55**, 2093 (1989).

14. M. A. Kinch, S. R. Borrello, and A. Simmons, Infrared Phys. **17**, 127 (1977).

15. W. R. Dyer and D. Duston, Electrochemical Society Proceedings **PV97-33**, 1 (1997).

16. C. G. Bethea, B. F. Levine, M. T. Asom, R. E. Leibengnth, J. W. Stayt, K. G. Glogovsky, R. A. Morgan, J. D. Blackwell, and W. J. Parrish, IEEE Trans. Electron Devices **40**, 1957 (1993).

17. W. A. Beck, J. W. Little, A. C. Goldberg, and T. S. Faska, "Quantum Well Infrared Transition Physics and Devices," NATO ASI Series, eds. H. C. Liu, B. F. Levine, and J. Y. Anderson, **270**, 55, Kluwer, Dordrecht (1994).

18. S.D. Gunapala, J. K. Liu, M. Sundaram, J. S. Park, C. A. Shott, T. Hoelter, T. I. Lin, S. T. Massie, P. D. Maker, R. E. Muller, and G. Sarusi, Electrochemical Society Proc. **95**, 55, The Electrochemical Society, Inc., Pennington, NJ (1995).

19. S.D. Gunapala, S. V. Bandara, J. K. Liu, W. Hong, M. Sundaram, P. D. Maker, and R. E. Muller, Electrochemical Society Proc. **PV97-33**, 14 (1997).

20. I. H. Campbell, I. Sela, B. K. Laurich, D. L. Smith, C.R. Bolognesi, L. A. Samoska, A. C. Gossard, and H. Kroemer, Appl. Phys.Lett. **59** 846 (1991).

21. P. M. Young, C. H. Grein, H. Ehrenreich, and R. H. Miles, J. Appl. Phys. **74**, 4774 (1993).

22. G. M. Williams, J. Appl. Phys. **77**, 4153 (1995).

23. C. H. Grein, M. E. Flatte, H. Ehrenreich, and R. H. Miles, R. H. Miles, J. Appl. Phys. **77**, 4156 (1995).

24. H. Ehrenreich, C. H. Grein, R. H. Miles, and M. E. Flatte, J. Appl. Phys. **80**, 2545 (1996).

25. C. H. Grein, P. M. Young, M. E. Flatte, and H. Ehrenreich, J. Appl. Phys. **78**, 7143 (1995).

26. J. L. Johnson , L. A. Samoska, A. D. Gossard, J. L. Merz, M. D. Jack, G. R. Chapman, B. A. Baumgratz, K. Kosai, and S. M. Johnson, J. Appl. Phys. **80**, 1116 (1996).

27. C. H. Grein and H. Ehrenreich, J. Appl. Phys. **82**, 6365 (1997).

28. H. Mohseni, J. Wojkowski, M. Razeghi, G. Brown, and W. Mitchel, IEEE J. Quantum Electronics **35**, 1041 (1999).

29. G. J. Brown, F. Szmulowicz, R. Linville, A. Saxler, K. Mahalingham, Chih-Hsiang Lin, C. H. Kuo, and W. Y. Hwang, IEEE Photonics Tech. Lett., **12**, 684 (2000)

30. S. S. Li, Materials Chemistry and Physics **50**, 188 (1997).

31. S. D. Gunapala, J. S. Park, G. Sarvsik, T. L. Lin, J. K. Liu, P. D. Maker, R. E. Muller, C. A. Shott, and T. Hoelter, IEEE Trans. Electron Devices **ED-44**, 45 (1997).

32. S. D. Gunapala, S. V. Bandara, J. K. Liu, E. M. Luong, N. Stetson, C. A. Shott, J. J. Bock, S. B. Rafol, J. M. Mumolo, M. J. McKelvey, IEEE Trans. Electron Devices **ED-47**, 326 (2000).

33. L. T. Claiborne, Proc. SPIE **2999**, 94 (1997).

34. T. N. Casselman, Proc. SPIE **2999**, 2 (1997).

35. M. Z. Tidrow, J. C. Chiang, and S. S. Li, and K. Bacher, Appl. Phys. Lett. **70**, 859 (1997).

36. J. C. Chiang and S. S. Li, M.Z. Tidrow, P. Ho, M. Tsai and C. P. Lee, Appl. Phys. Lett. **69**, 2412 (1996).

37. J. Lee, S. S. Li, M. Z. Tidrow, W. K. Liu, and K. Bacher, Appl. Phys. Lett. **75**, 3207 (1999).

38. J. Lee, S. S. Li, M. Z. Tidrow, and W. K. Liu, Electronics Lett. **36**, 1508 (2000).

39. K. K. Choi, J. Appl. Phys., 73 (1993) 5230.

40. Y. C. Wang and S. S. Li, J. Appl. Phys. **75**, 8168 (1994).

41. David J. Griffiths, "Introduction to Quantum Mechanics," Prentice-Hall, Inc., Englewood Cliff, NJ (1995).

42. G. Bastard, Phys. Rev. **B-245**, 5693 (1981).

43. D. Delagebeaudeuf, P. Deleckyse, P. Etienne, J. Massiers, M. Laviron, J. Chaplart, and T. Linh, Electronics Lett. **18**, 85 (1982).

44. I. Hase, H. Kawai, K. Kaneko, and K. Watanabe, Electronics Lett. **20**, 491 (1984).

45. P. J. Price, IBM J. Res. Develop. **17**, 39 (1973).

46. M. Artaki and K. Hess, Superlattice and Microstructures **1**, 489 (1985).

47. Ajoy K. Ghatak, K. Thyagarajan, and M. R. Shenoy, IEEE J. Quantum Electronics **23**, 1524 (1988).

48. Y. H. Wang, S. S. Li, J. Chu, and Pin Ho, Appl. Phys. Lett. **64**, 727 (1994).

49. Y. H. Wang, J. Chu, S. S. Li, and Pin Ho, J. Appl. Phys. **76**, 6009 (1994).

50. J. Chu, S. S. Li, and Pin Ho, Appl. Phys. Lett. **69**, 1258 (1996).

51. L. H. Peng, J. H. Smet, T. P. E. Broekaert, and C. G. Fonstad, Appl. Phys. Lett. **62**, 2413 (1993).

52. G. Karunasri, J. S. Park, J. Chen, R. Shih, J. F. Scheihing, and M. A. Dodd, Appl. Phys. Lett. **67**, 2600 (1995).

53. J. W. Matthews and A. E. Blakeslee, J. Crys. Growth **27**, 118 (1974).

54. G. E. Bir and G. E. Pikus, "Symmetry and Strain-Induced Effects in Semiconductors," J. Wiley, New York (1974).

55. S. H. Pan, H. Shen, Z. Hang, F. H. Pollak, W. Zhuang, Q. Xu, A. P. Roth, R. A. Masut, C. Lacelle, and D. Morris, Phys. Rev. **B-38**, 3375 (1988).

56. D. Ahn and S. L. Chuang, IEEE J. Quantum Electron. **QE-23**, 2196 (1987).

57. G. Hasnain, B. F. Levine, C. G. Bethea, R. A. Logan, J. Walker, and J. Malik, Appl. Phys. Lett. **54**, 2515 (1989).

58. Y. C. Wang and S. S. Li, J. Appl. Phys. **75**, 582, (1994).

59. H. Schneider, E. C. Larkins, J. D. Ralston, K. Schwarz, F. Fuchs, and P. Koidl, Appl. Phys. Lett. **63**, 782 (1993).

60. S. D. Gunapala, B. F. Levine, L. Pfeiffer, and K. West, J. Appl. Phys. **69**, 6517 (1991).

61. E. L. Derniak and D. G. Crowe, "Optical Radiation Detectors, " Wiley, New York (1984).

62. H. C. Liu, Appl. Phys. Lett. **60**, 1507 (1992); **61**, 2703 (1992).

63. W. A. Beck, Appl. Phys. Lett. **63**, 3589 (1993).

64. A. Zussman, B. F. Levine, J. M. Kuo, and J. de Jong, J. Appl. Phys. **70**, 5101 (1991).

65. Yimin Huang and Chenhsin Lien, and Tan-Fu Lei, J. Appl. Phys. **74**, 2598 (1993).

66. Yimin Huang and Chenhsin Lien, J. Appl. Phys. **78**, 2700 (1995).

67. J. C. Chiang, S. S. Li, and A. Singh, Appl. Phys. Lett. **71**, 3546 (1997).

68. S.D. Gunapala, S. V. Bandara, J. K. Liu, W. Hong, M. Sundaram, P. D. Maker, R. E. Muller, C. A. Shott, and R. Carralejo, Intersubband Transitions in Quantum Wells: Physics and Devices, eds. S. S. Li and Y. K. Su, Kluwer Academic, 193 (1998).

69. L. S. Yu, Y. H. Wang, Sheng S. Li, and P. Ho, Appl. Phys. Lett. **60**, 992 (1992).

70. E. L. Derniak and D. G. Crowe, "Optical Radiation Detectors," Wiley, New York, (1984).

71. D. C. Wang, G. Bosman, and Sheng S. Li, Appl. Phys. Lett. **8**, 2532 (1997).

72. R. H. Miles and D. H. Chow, Long Wavelength Infrared Detectors: ed. M. Razeghi, Gordon and Breach Science Publishers, 397 (1996).

73. A. Rogalski, Infrared Physics & Technology **38**, 295 (1997).

74. D.L. Smith and D. Maihiot, J.Appl. Phys. **62**, 2545 (1987).

75. D. H. Chow, R. H. Miles, J. R. Söderström, and T. C. McGill, Appl. Phys. Lett. **56**, 1418 (1990).

76. Su-Huai Wei and Alex Zunger, Phys. Rev. B **52**, 12039 (1995).

77. C. Jenner, E. Corbin, B.M. Adderley and M. Jaros, Semicond. Sci. Technol. **13**, 359 (1997).

78. E. R. Youngdale, J. R. Meyer, C. A. Hoffman, F. J. Bartoli, C. H. Grein, P. M. Yound, H. Ehrenreich, R. H. Miles, and D. H.Chow, Appl. Phys. Lett. **64**, 3160 (1994).

79. E. O. Kane, Physics of III-V compounds **1**, Academic Press, New York, 75 (1966).

80. G. E. Pikus and G. L. Bir, Fiz. Tverd. Tela. **1**, 1642 (1959).

81. F. H. Pollak and M. Cardona, Phys. Rev. **172**, 816 (1967).

82. D. N. Talwar, J. P. Loehr, and B. Jogai, Phys. Rev. B **49**, 10345 (1994).

83. B. Jogai and D. N. Talwar, Phys. Rev. B **54**, 14524 (1996).

84. G. C. Osbourn, J. Appl. Phys. **53**, 1586 (1982).

85. G. L. Bir and G.E. Pikus, "Symmetry and Strain Effects in Semiconductors," John Wiley and Sons, New York, (1974).

86. A. Rose, "Concepts in Photoconductivity and Allied Problems", Interscience, New York, (1963).

87. M. A. Kinch and S. R. Borrello, Infrared Physics **15**, 111 (1975).

88. J. Piotrowski, W. Gawron, and Z. Djuric, Optical Engineering **33**, 1413 (1994).

89. D. Long, Optical and Infrared Detectors, ed. R. J. Keyes, Springer, New York (1980).

90. H. Mohseni, M. Razeghi, G. Brown, and Y. S. Park, Appl. Phys. Lett. **78**, 2107 (2001).

91. H. Mohseni and M. Razeghi, IEEE Photonics Tech. Lett. **13**, 517 (2001).

92. D. K. Arch, G. Wicks, T. Tonaue, and J. L. Staudenmann, J. Appl. Phys. **58**, 3933 (1985).

93. L. R. Ram-Mohan, K. H. Yoo, and R. L. Aggarwal, Phys. Rev. B **38**, 6151 (1988).

94. J. N. Tu, J. W. Mayer, and L. C. Feldman, Electronic Thin Film Science for Electrical Engineers and Materials Scientist, Macmillan, New York, (1992).

95. G. J. Brown, F. Szmulowicz, R. Linville, A. Saxler, K. Mahalingham, C. H. Lin, C. H. Kuo, and W. T. Hwang, IEEE Photonics Tech. Lett. **12**, 684 (2000).

96. J. W. Matthews and A. E. Blakeslee, J. Cryst. Growth **32**, 265 (1976).

97. H. Mohseni, A. Tahraoui, J. Wojkowski, M. Razeghi, G. J. Brown, W. C. Mitchel, and Y. S. Park, Appl. Phys. Lett., **77**, 1572 (2000).

98. H. Mohseni, E. Michel, Jan Sandoen, M. Razeghi, W. Mitchel, and G. Brown, Appl. Phys. Lett., **71**, 1403 (1997).

99. Y. Wei, A. Gin, M. Razeghi, and G. J. Brown, Appl. Phys. Lett., **80**, 3262 (2002)

100. M. H. Young, D.H. Chow, A. T. Hunter and R. H. Miles, Appl. Surface Science, **123-124**, 395 (1998)

101. B. L. Carter, E. Shaw, J. T. Olesberg, W. K. Chan, T. C. Hasenberg and M. E. Flatté, Electronics Lett. **36**, 1301 (2000).

102. C. A. Wang, H. K. Choi, D. C. Oakley, and G. W. Charache, J. Crystal Growth **195**, 346 (1998).

103. H. K. Choi, C. A. Wang, G. W. Turner, M. J. Manfra, D. L. Spears, G. W. Charache, L. R. Danielson, and D. M. Depoy, Appl. Phys. Lett. **71**, 3758 (1997).

104. S. S. Li, "Semiconductor Physical Electronics," Plenum, New York, (1993).

105. B. Zhang, T. Zhou, H. Jiang, Y. Ning, Y. Jin, Electronics Lett. **31**, 830 (1995).

106. E. Tournie, J. L. Lazzari, E. Villemain, A. Joulie, L. Gouskov, M. Karim, and I. Salesse, Electronics Lett. **27**, 1237 (1991).

107. B. Wu, G. Xia, Z. Li, and J. Zhou, Appl. Phys. Lett. **80**, 1303 (2002).

108. S. D. Gunapala and S. V. Bandara, Semiconductors and Semimetals, H. C. Liu and F. Capasso, Eds. San Diego, Ca: Academic, **62**, 197 (2000).

109. W. R. Dyer, Electrochemical Society Proceedings **99-22**, 425 (1999).

110. W. A. Beck and T. S. Faska, Proc. SPIE **2744**, 193 (1996).

111. P. L. McCarley, M. A. Massie, C. R. Baxter, and B. L. Huynh, Proc. SPIE **3360**, 13 (1998).

112. S. D. Gunapala, S. V. Bandara, A. Singh, J. K. Liu, S. B. Rafol, E. M. Luong, J. M. Mumolo, N. Q. Tran, D. Z.–Y. Ting, J. D. Vincent, C. A. Shott, J. Long, P. D. LeVan, Electron Devices, **47**, 963 (2000).

113. S. D. Gunapala, S. V. Bandara, J. K. Liu, S. B. Rafol, J. M. Mumolo, Electron Devices, **50**, 2353 (2003).

114. J. Jiang, S. Tsao, K. Mi, M. Razeghi, C. J. Brown, C. Jelen, and M. Z. Tidrow, Infrared Physics and Technology, article in press, (2004).

115. M. Razeghi, A. Gin, Y. Wei, J. Bae, and J. Nah, Microelectronics Journal, **34**, 405 (2003).

116. J. H. Lee, Ph. D dissertation at Univ. of Florida, 92 (2000).

117. J. Y. Anderson and L. Lundqvist, Appl. Phys. Lett., **59**, 857 (1991).

118. J. Y. Anderson, L. Lundqvist, and Z. F. Paska, Appl. Phys. Lett., **58**, 2264 (1991).

119. E. Yablonovitch and G. D. Cody, IEEE Trans. Electron. Devices **ED-29**, 300 (1982).

120. C. J. Chen, K. K. Choi, M. Z. Tidrow, and D. C. Tsui, Appl. Phys. Lett. **68**(11), 1446 (1996).

121. K. K. Choi, "The physics of quantum well infrared photodetectors", World Scientific (1997).

122. E. Costard, P. Bois, X. Marcadet, F. Audier, and E. Herniou, Proc. SPIE **3398**, 82 (1999).
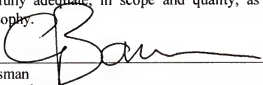
BIOGRAPHICAL SKETCH

Junhee Moon was born in Seoul, Korea, on September 13, 1969. He received a Bachelor of Engineering degree at the Department of Electrical Engineering from Hanyang University, Seoul, Korea, in February 1993. After his graduation, he served in the Second Corps of the Korean Army for 26 months.

He received a Master of Engineering degree at the Department of Electrical and Computer Engineering from the University of Florida, Gainesville, Florida, in May 1999. After his graduation, he extended his research and continued working towards his Ph.D. degree at the University of Florida. His Ph.D. research has been focused on the development of a multicolor quantum well infrared photodetector and type II superlattice infrared detectors.
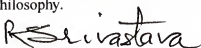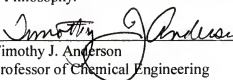
I certify that I have read this study and that in my opinion it conforms to acceptable standards of scholarly presentation and is fully adequate, in scope and quality, as a dissertation for the degree of Doctor of Philosophy.

Sheng S. Li, Chair
Professor of Electrical and Computer Engineering

I certify that I have read this study and that in my opinion it conforms to acceptable standards of scholarly presentation and is fully adequate, in scope and quality, as a dissertation for the degree of Doctor of Philosophy.

Gijs Bosman
Professor of Electrical and Computer Engineering

I certify that I have read this study and that in my opinion it conforms to acceptable standards of scholarly presentation and is fully adequate, in scope and quality, as a dissertation for the degree of Doctor of Philosophy.
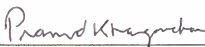
Ramakant Srivastava
Professor of Electrical and Computer Engineering

I certify that I have read this study and that in my opinion it conforms to acceptable standards of scholarly presentation and is fully adequate, in scope and quality, as a dissertation for the degree of Doctor of Philosophy.

Timothy J. Anderson
Professor of Chemical Engineering

This dissertation was submitted to the Graduate Faculty of the College of Engineering and to the Graduate School and was accepted as partial fulfillment of the requirements for the degree of Doctor of Philosophy.

December 2004

Pramod Khargonekar
Dean, College of Engineering

Kenneth J. Gerhardt
Interim Dean, Graduate School